OPEN ACCESS



The Cool Circumgalactic Medium of Low-redshift Star-forming Galaxies. I. Empirical Model and Mean Properties

Yakov Faerman and Jessica K. Werk Astronomy Department, University of Washington, Seattle, WA 98195, USA; yakov.faerman@gmail.com
Received 2023 January 30; revised 2023 July 21; accepted 2023 August 11; published 2023 October 11

Abstract

We present an analytic model for the cool, $T\sim 10^4$ K, circumgalactic medium (CGM), describing the gas distribution, and thermal and ionization states. Our model assumes (total) pressure equilibrium with the ambient warm/hot CGM, photoionization by the metagalactic radiation, and allows for nonthermal pressure support, parameterized by the ratio of thermal pressures, $\eta=P_{\rm hot,th}/P_{\rm cool,th}$. We apply the model to the COS-Halos measurements and find that a nominal model with $\eta=3$, gas distribution out to $r\approx 0.6R_{\rm vir}$, and $M_{\rm cool}=3\times 10^9\,M_{\odot}$, corresponding to a volume filling fraction of $f_{\rm V,cool}\approx 1\%$, reproduces the H I and low/intermediate metal ions (C II, C III, Si II, Si III, and Mg II) mean column densities. Variation of ± 0.5 dex in η or $M_{\rm cool}$ encompasses $\sim 2/3$ of the scatter between objects. Our nominal model underproduces the measured C IV and Si IV columns, and these can be reproduced with (i) a cool phase with $M_{\rm cool}\sim 10^{10}\,M_{\odot}$ and $\eta\approx 5$, or (ii) cooling or mixing gas at intermediate temperatures, with $M\sim 1.5\times 10^{10}\,M_{\odot}$ and occupying $\sim 1/2$ of the total CGM volume. For cool gas with $f_{\rm V,cool}\approx 1\%$, we estimate an upper limit on the cloud sizes, $R_{\rm cl}\lesssim 0.5$ kpc. Our results suggest that for the average galaxy CGM, the mass and nonthermal support in the cool phase are lower than previously estimated, and extreme scenarios are not necessary. We estimate the rates of cool gas depletion and replenishment, and find accretion onto the galaxy can be offset, allowing $\dot{M}_{\rm cool}\approx 0$ over long timescales.

Unified Astronomy Thesaurus concepts: Circumgalactic medium (1879); Galaxy structure (622); Galaxy evolution (594); Quasar absorption line spectroscopy (1317); Intergalactic medium (813); Galaxy formation (595); Interstellar medium (847); Galactic and extragalactic astronomy (563); Galaxy processes (614)

Supporting material: tar.gz file

1. Introduction

Absorption observations of the low-redshift circumgalactic medium (CGM) reveal massive, metal-enriched, and highly multiphase halos, with ions from Mg II to O VIII, tracing temperatures from $\sim 10^4$ K to $\sim 10^6$ K (Tumlinson et al. 2017). The physical conditions in the CGM are set by the same processes that affect the evolution of galaxies and determine their morphologies, including accretion from the intergalactic medium (IGM) into the halo and onto the galaxy, gas stripping from satellite galaxies, and feedback from the galaxy, in the form of winds and radiation from supernovae and active galactic nuclei (AGNs).

The warm/hot CGM has been studied by many recent works presenting different physical models and exploring various assumptions and scenarios (Faerman et al. 2017; Mathews & Prochaska 2017; Qu & Bregman 2018a, 2018b; Lochhaas et al. 2018; McQuinn & Werk 2018; Stern et al. 2018, 2019; Voit 2019; Faerman et al. 2020). These models, addressing the gas spatial distribution, kinematics, thermodynamics, and ionization states, enable relating the CGM observables to the gas physical properties and the processes that shape the CGM and the galaxy. They also produce different gas distributions that may be tested with future observations in the radio (SZ, fast radio bursts), and UV/X-ray absorption and emission (see P. Singh et al. 2023, in preparation, for a comparison between models).

Original content from this work may be used under the terms of the Creative Commons Attribution 4.0 licence. Any further distribution of this work must maintain attribution to the author(s) and the title of the work, journal citation and DOI.

The cool component of the CGM, at $T \sim 10^4$ K, is not less interesting, as it may dominate the accretion from the CGM onto the galaxy (e.g., Ribaudo et al. 2011; Oppenheimer et al. 2018a; Ramesh et al. 2023c), replenishing the ISM and providing fuel for star formation and supermassive black hole (SMBH) growth (Putman et al. 2012; Somerville et al. 2015). Recent decades have seen significant progress in observational studies of the cool CGM. At low redshift, this phase is observed mainly in UV absorption, using the Hubble Space Telescope (HST) Cosmic Origins Spectrograph (COS; e.g., Prochaska et al. 2011; Stocke et al. 2013; Tumlinson et al. 2013; Werk et al. 2013; and see Piacitelli et al. 2022 for emission predictions). Measurements include both hydrogen transitions and metal lines, allowing estimation of the gas metallicity (e.g., Prochaska et al. 2017; Chen et al. 2018; Wotta et al. 2019; Berg et al. 2023) and showing that it is significantly metal-enriched. At higher redshifts, cool gas is observed both from space and the ground, in absorption (Hennawi & Prochaska 2013; Rudie et al. 2013; Lehner et al. 2014, 2022) and emission (Cantalupo et al. 2014; Borisova et al. 2016; Cai et al. 2018). Neutral and molecular gas at temperatures below 10⁴ K is also detected (Neeleman et al. 2015, 2016).

These observations motivated many theoretical studies, with different approaches, including analytic estimates for the gas formation and evolution timescales (Maller & Bullock 2004), phenomenological modeling (Stern et al. 2016; Haislmaier et al. 2021; Sameer et al. 2021, and see Hafen et al. 2023), toy models addressing different scenarios for the gas kinematics (Afruni et al. 2019; Lan & Mo 2019), and numerical simulations of gas physics, including the effects of radiative processes, turbulence, magnetic fields, and cosmic rays

(McCourt et al. 2012; Armillotta et al. 2017; Ji et al. 2019; Butsky et al. 2020; Sparre et al. 2020; Gronke et al. 2022).

Larger, zoom-in, and cosmological simulations are crucial for capturing the effects of the cosmic web and galaxy evolution on the structure and thermodynamics of the CGM (e.g., Nelson et al. 2018; Oppenheimer 2018; Hafen et al. 2019; Roca-Fàbrega et al. 2019; Appleby et al. 2021; Damle et al. 2022; Ramesh et al. 2023b). However, these numerical experiments face several challenges when used to study the CGM. First, the gas properties vary significantly with the subgrid recipes employed to model stellar and black hole feedback (Kelly et al. 2022; C. Strawn et al., 2023 in preparation), tuned to reproducing the observed galactic stellar populations. Second, the spatial resolution in the CGM is often limited. Recent studies that focused more attention on the CGM by increasing the spatial resolution (Hummels et al. 2019; Peeples et al. 2019; van de Voort et al. 2019; and see also Nelson et al. 2020) showed that while the properties of the volume-filling warm/hot gas may be converged, this is not the case for the cool CGM properties and observables. Finally, the effects of small-scale physical processes are often not included in these simulations and may be especially significant for the cool gas (Hopkins et al. 2020).

Given these challenges, it is interesting to employ analytic models to study the cool phase of the CGM. These can test a variety of physical scenarios and processes, and be applied to observations to address interesting questions that remain open about this phase—what is its spatial distribution, thermal properties, and morphology? What are the physical processes that set these properties? How does the cool gas evolve and interact with the galaxy?

In this work, we present a physically motivated phenomenological model for the cool CGM in combination with the detailed warm/hot CGM model developed in FSM20. We address the spatial distribution of the cool gas and its ionization state, including the effects of photoionization and considering nonthermal support. We apply this model to the COS-Halos measurements of HI and metal ions to estimate the cool gas extent, density, and mass in an average star-forming galaxy. This is the first study performing forward-modeling of the observed metal ion column densities in the cool CGM within the context of a physically motivated model for the warm/hot gas.

This manuscript is structured as follows. We discuss the observational data we model and our goals in Section 2, describe our model setup in Section 3, and present our main results for the column densities of cool gas in an average galaxy in Section 4. We then show additional variations of the model in Section 5 and provide tools for inferring gas properties in individual sight lines. We address some uncertainties of our model in Section 6, discuss the morphology and the depletion-replenishment cycle of cool CGM in Section 7, and summarize in Section 8.

2. Goals and Observational Data

In this work we model the hydrogen and metal ion column densities in the CGM of star-forming galaxies at low redshifts, measured as part of the COS-Halos survey. We now briefly describe the survey, the data, and the goals of our study.

The COS-Halos survey used the COS on board the HST to study gas around L^* galaxies at redshifts $0.1 \lesssim z \lesssim 0.4$ (Tumlinson et al. 2011; Werk et al. 2012). The survey, carried

out during HST Cycle 17, the first cycle in which COS was available, remains the most complete CGM survey of L* galaxies at z < 1 probing the inner CGM, at impact parameters of up to $\sim 0.6 R_{\rm vir}$ (Werk et al. 2013). It revealed that the CGM is extended, massive, and highly multiphase, with ions ranging from low (Mg II, C II, Si II), through intermediate species (C III, Si III), and up to even more ionized gas, traced by higher ions (N V and O VI). The survey also measured the galaxy properties, including stellar masses and star formation rates (SFRs). Motivated by the measurements of high O VI column densities in star-forming galaxies (specific star formation rate > 10⁻¹¹ yr⁻¹), FSM17 and FSM20 constructed models for the warm/hot CGM, which successfully reproduced the observed O VI column density profile, as well as the O VII and O VIII column densities measured in the Milky Way (MW) in the X-ray (Bregman & Lloyd-Davies 2007; Gupta et al. 2012; Fang et al. 2015).

In this work, we extend the FSM20 framework by adding a cool, photoionized component to the CGM. We then apply this model to the COS-Halos measurements of H I and the low/ intermediate metal ions to infer the model parameters consistent with observations and constrain the gas properties, such as density and mass. For this purpose, we use the same subsample of star-forming galaxies addressed by FSM20. The column densities are reported by Werk et al. (2013) and Prochaska et al. (2017), and for the metal ions, we focus on the C II-C IV, Si II-Si IV, and Mg II columns. These ions span a range of ionization potentials and probe different gas densities.² The columns modeled in this work are the total column densities measured for each sight line, summed over all detected subcomponents. We plot the measured columns and their errors in Figures 3-6, and provide the underlying data in Table A1 in Appendix A.

One notable feature of the low ion measurements is the scatter in column densities between different galaxies at a given (projected) normalized distance from the galaxy.³ For example, the H I columns (Figure 3) have a scatter of >1 dex at impact parameters $h < 0.4~R_{\rm vir}$. The metal ions (Figures 4–6) can have both upper and lower limits, differing by 0.5–1.0 dex, at similar $h/R_{\rm vir}$. This is in contrast to the O VI column densities measured for these galaxies (Tumlinson et al. 2011), which show a much smaller scatter between different objects in the sample (see Figure 10 in FSM20).

Our main goal in this work is to reproduce the typical, mean column densities of H I and metal ions, and their scatter. This is a first-order approximation, addressing the properties of the cool gas in an average star-forming galaxy. For easier comparison to our models, we bin the individual measurements, and the

¹ Other studies and data sets at low-z span different halo masses, galaxy morphologies, and environments (Stocke et al. 2013; Bordoloi et al. 2014; Borthakur et al. 2015; Johnson et al. 2015; Keeney et al. 2017; Burchett et al. 2019; Chen et al. 2020; Zahedy et al. 2021; Zheng et al. 2023). Data from the CGM^2 survey, for example, extend to larger impact parameters, beyond R_{vir} (Wilde et al. 2021; Tchernyshyov et al. 2022).

² Outputs for similar ions of other elements (nitrogen, sulfur, and iron, for example) are calculated and are not shown for compactness of presentation.

In this work we address the column densities as functions of the physical projected distances normalized by the halo virial radii. In our model we use the MW mass profile and normalize the radial and projected distances by $R_{\rm vir} = 258$ kpc (see FSM17). The median virial radius of the galaxies in our sample is very similar, with $R_{\rm vir} \approx 260$ kpc. The data in the attached files provide both physical and normalized distances.

⁴ The columns of individual objects, which may be related to the galaxy properties and histories, will be the focus of a separate study.

binned data are plotted as large black and gray markers, with the errors bars representing the 1σ scatter in each bin. For the purpose of binning, we treat upper and lower limits as measurements, unless all of the data in a bin are upper or lower limits. The vertical thin dashed lines in the left panel of each figure show the boundaries of the bins.

We note a few other points. First, while the small-scale morphology and kinematics of the cool gas are beyond the scope of this work, in Section 7.1 we show that our model provides upper limits on the gas cloud size. Second, our model is agnostic to the origin or formation channel of the cool gas, and we discuss these briefly in Section 7.2. With these goals and reservations in mind, we now present our model setup for the cool gas.

3. Model Setup

Two important inferences have been made from modeling the COS-Halos absorption measurements: (i) the cool gas densities are lower than those expected from thermal pressure equilibrium with the hot phase (Werk et al. 2014, hereafter W14), and (ii) the cool gas mass, traced by H I, is $M_{\rm cool} \gtrsim 10^{10}\,M_{\odot}$, a significant fraction of the total baryons associated with these halos (W14; Prochaska et al. 2017, hereafter P17). We revisit these two points in this work and aim to quantify what gas densities and masses are required to reproduce the measured absorption. To do this, we add a cool gas phase to the FSM20 model for the warm/hot CGM, and we now describe the parameters we choose for constructing the cool gas distribution.

First, we address nonthermal pressure support, setting the gas density. The high detection rate of cool gas in the CGM suggests that it is abundant and long-lived on large scales, rather than a transient phase. On small scales, cool gas clouds can be either (i) approximately stable, or (ii) constantly being destroyed and replenished, leading to an approximately constant amount of cool gas. Previous works estimated large masses of cold gas in the CGM, and the second scenario is more challenging to sustain in terms of mass and energy input. Thus, in this work we assume that the cool CGM clouds are in local pressure equilibrium with the warm/hot phase, and are not disrupted on short timescales.⁵ This assumption can be written as $P_{\text{hot,tot}}(r) = P_{\text{cool,tot}}(r) \equiv P_{\text{tot}}(r)$. In FSM20, the amount of nonthermal pressure in the warm/hot phase is given by the parameter $\alpha_{\text{tot}} = P_{\text{hot,tot}}/P_{\text{hot,th}} \equiv \alpha_{\text{hot}}$ (see also Equation (2) in Faerman et al. 2022). In this work, we allow the cool phase to have a separate nonthermal pressure component, $\alpha_{\rm cool} = P_{\rm cool,tot}/P_{\rm cool,th}$, and define the ratio

$$\eta \equiv \alpha_{\rm cool}/\alpha_{\rm hot} = P_{\rm hot,th}/P_{\rm cool,th},$$
(1)

where we used total pressure equilibrium between phases. For a given distribution of warm/hot gas, setting η allows us to write the cool gas density at a given distance r from the center of the halo (i.e., from the galaxy)

$$n_{\rm cool}(r) = n_{\rm hot} \frac{\alpha_{\rm hot}}{\alpha_{\rm cool}} \frac{T_{\rm hot}}{T_{\rm cool}} = \frac{P_{\rm hot,th}/k_{\rm B}}{\eta T_{\rm cool}},$$
 (2)

where $P_{\rm hot,th}/k_{\rm B} = n_{\rm hot}T_{\rm hot}$, and $T_{\rm cool}$ is the temperature of the cool phase, set by heating/cooling equilibrium with the

metagalactic radiation field (MGRF),⁶ and it depends on the gas density and metallicity. To obtain $n_{\rm cool}$, we assume the metallicity at a given radius and solve for the density and temperature iteratively. We start by inserting $T_{\rm cool}=10^4$ K into Equation (2) and solve for the density. We then use Cloudy 17.00 (Ferland et al. 2017) to obtain the equilibrium temperature for this density, adopting the Haardt & Madau (2012, hereafter HM12) MGRF, and repeat the calculation until the temperature converges. For the densities estimated for the cool CGM, $10^{-1} < n_{\rm cool}/{\rm cm}^{-3} < 10^{-5}$ (W14, P17) and at a constant metallicity, $T_{\rm cool}$ varies very weakly with n. We show $T_{\rm cool}$ as a function of radius for different values of η in the right panel of Figure 1.

Given the weak variation of temperature with radius, the density profile of the cool gas is set mainly by η and by the pressure in the warm/hot phase. The nonthermal support in the warm/hot phase varies with radius, and for the fiducial FSM20 model it is in the range $\alpha_{hot} \approx 1.5-3$. In this work, we use η , rather than α_{cool} , as one of the parameters for our model of the cool gas, and assume η to be constant with radius, for simplicity. For $\eta = 1$, pressure equilibrium between the two phases implies thermal pressure equilibrium, and the ratio of densities is given by the inverse of the temperatures ratio. $\eta > 1$ lowers the density in the cool gas, and it is motivated empirically by the analysis in W14 (see their Section 5.3 and Figure B1 here). Theoretically, higher nonthermal support in the cool phase is expected for magnetic fields, for example, if the cool gas forms from the hot component (see Nelson et al. 2020; Ramesh et al. 2023a) and the magnetic flux is frozen into the condensing clouds, or for other mechanisms that couple more strongly to denser gas.

Second, we define the cool gas volume filling fraction as

$$f_{\rm V,cool} \equiv dV_{\rm cool}/dV,$$
 (3)

where $dV_{\rm cool}$ is the volume occupied by cool gas and $dV = 4\pi r^2 dr$ is the total volume, both in a shell at a given radius. We then define the spatial distribution of the cool gas by setting $f_{\rm V,cool}$ to be nonzero in a radial range $r_1 < r < r_2$, where $r_1 = 0.05R_{\rm vir}$ and $r_2 < r_{\rm CGM}$. The inner boundary is chosen to exclude the region close to the galaxy, where winds/outflows and interaction with the galaxy may be dominant, requiring a more detailed model (see Fielding & Bryan 2022, for example). As shown in Figures 3–6, the observations we model in this work probe impact parameters up to $\sim 0.6R_{\rm vir}$.

The volume filling fraction, together with the gas density, set the mass distribution and the total mass in the cool phase:

$$M_{\text{cool}} = \int_0^{r_{\text{CGM}}} \rho_{\text{cool}}(r) dV_{\text{cool}}$$

$$= 4\pi \int_{r_1}^{r_2} f_{\text{V,cool}}(r) \bar{m}(r) n_{\text{cool}}(r) r^2 dr, \tag{4}$$

where \bar{m} is the mean mass per particle, calculated as a function of radius given the gas ionization state. In this work, we assume

⁵ However, balance does not have to be perfect, which may lead to a slow depletion of cool gas, and we discuss possible replenishment mechanisms in Section 7.2.

⁶ In this work we assume the cool gas heating and photoionization are dominated by the MGRF. We discuss the effect of different MGRF models and a possible contribution of galactic radiation in Section 6.2.

 $^{^{7}}$ At $n_{\rm cool} < 10^{-5}$ cm⁻³, the gas equilibrium temperature has a stronger variation with density. As we see in the next section, the cool gas densities in our models are above this limit.

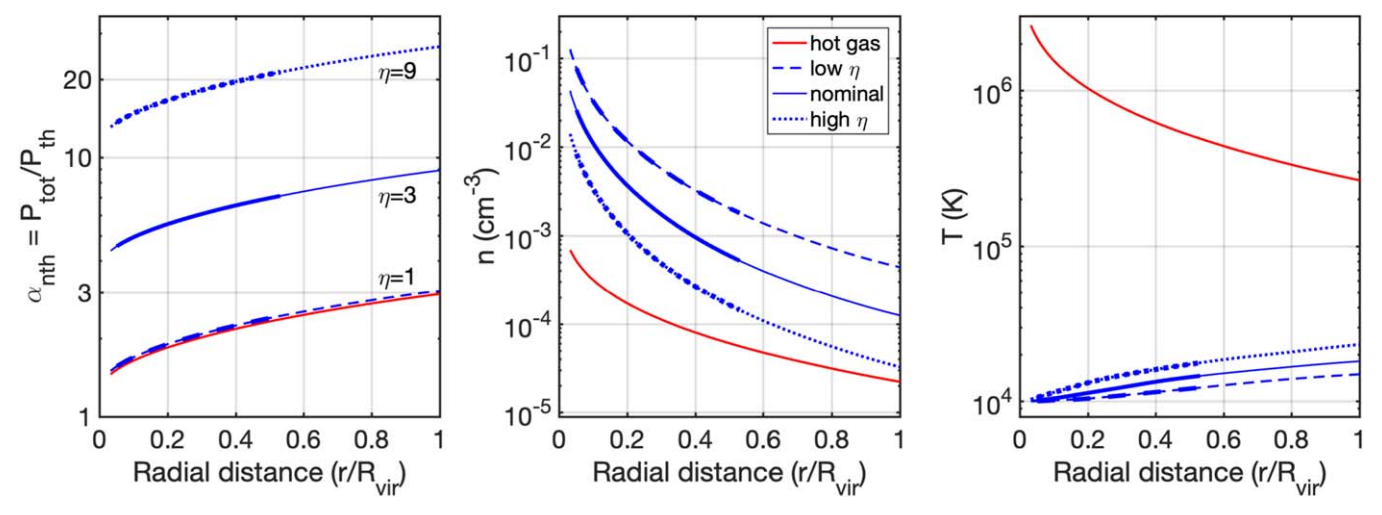


Figure 1. Gas thermal properties: nonthermal support (left), density (middle), and temperature (right). The red curves show the properties of the warm/hot gas in the FSM20 fiducial model, and the blue curves are for the cool phase described in this work. The solid curves show the nominal model, and the models in the radius and mass sets (#2 and #3) have the same profiles. The dashed (dotted) curves show models with low (high) nonthermal support (pressure set, #1). The thick part of each curve shows the gas nominal spatial extent, $r_2 = 0.55R_{\rm vir}$. Left: $\eta \equiv \alpha_{\rm cool}/\alpha_{\rm hot}$ is constant with radius, and the actual amount of nonthermal support, given by $\alpha_{\rm cool}$, follows the nonthermal support in the warm/hot gas. Middle: for a given total pressure profile set by the hot gas, higher nonthermal support in the cool phase corresponds to lower volume density. Right: the gas temperature, set by heating/cooling equilibrium with the MGRF, depends on the gas density and varies with radius and, to a smaller extent, between models (see Section 4.1 for details). The model outputs used in this figure are available in machine-readable format.

a mass fraction of Y = 0.25 in helium, and $\mu \equiv \bar{m}/m_p$ ranges from 0.59 in fully ionized gas to 1.23 in neutral gas.

To compare our models with observations, we calculate the ion column densities as functions of the impact parameter. To do this, we use Cloudy to calculate the gas ionization state (i.e., ion fractions) assuming photoionization equilibrium in optically thin gas in the presence of the HM12 MGRF, for a range of gas densities and temperatures (see Section 6.2 for a discussion on the MGRF and optically thin gas). The H I column as measured by an external observer through the CGM at an impact parameter *h* from the galaxy is then given by

$$N_{\rm H\,I}(h) = \int_{s} n_{\rm cool}(r) f_{\rm V,cool}(r) f_{\rm H\,I}(r) ds, \tag{5}$$

where $f_{\rm H\,I}(r)$ is the neutral hydrogen fraction as a function of radius and $s=\sqrt{h^2-r^2}$ is the coordinate along the line of sight. For an assumed (relative to solar) metallicity profile Z'(r), the column for an ion of element X with abundance A_X is

$$N_{\text{ion}}(h) = \int_{\mathbb{R}} n_{\text{cool}}(r) f_{\text{V,cool}}(r) A_{\text{X}} Z'(r) f_{\text{ion}}(r) ds.$$
 (6)

In this work we use the Asplund et al. (2009) values for the solar metal abundances, with $A_{\rm C}=2.7\times10^{-4},~A_{\rm Si}=3.2\times10^{-5},$ and $A_{\rm Mg}=4.0\times10^{-5},$ for carbon, silicon, and magnesium, respectively. Next we apply this model to the data.

4. Model Demonstration: Basic

In this section we present three sets of model parameter combinations, in which we vary the gas physical properties, examine how these variations affect the gas observables—the H I and metal ions column densities—and how observations constrain the properties of the cool CGM.

First, we examine the amount of nonthermal pressure in the cool phase, set by η (see Equation (1)), and show how it affects the gas ionization state (pressure set, #1, Section 4.1). Second, we address the gas radial distribution and vary r_2 , the maximal

radius at which cool gas is present (radius set, #2, Section 4.2). To isolate the effect of these parameters on the column densities, we set the gas mass in these two sets to $M_{\rm cool} = 3.0 \times 10^9 \, M_{\odot}$ by adjusting the value of $f_{\rm V,cool}$, the gas volume filling fraction, between models (see Equation (4)). Finally, we vary $M_{\rm cool}$, asking what masses are needed to reproduce the measured columns (mass set, #3, Section 4.3).

As described in Section 3, we set η , $f_{V,cool}$, and the gas metallicity, Z', to be constant as functions of radius. In Section 5.3 we show how the measured column densities can be used to constrain these parameters for individual objects and lines of sight. In this work we adopt a value of Z'=0.3 solar, motivated by the median metallicity inferred for the COS-Halos absorbers by P17 9 (see also Wotta et al. 2016, 2019). We adopt the fiducial FSM20 parameters for the warm/hot gas distribution, and discuss how variation in the ambient pressure profile affects our results in Section 6.1. To calculate the ion fractions, we use the HM12 field at z=0.2, the median redshift of the galaxies in our sample, and in Section 6.2 we address a possible contribution from galactic radiation and the redshift evolution of the MGRF ionizing flux.

To allow for an easy comparison between the model sets, we define a nominal model—a single combination of parameters chosen to reproduce the binned data. We then present two variations on this model in the parameter that is being explored in each set. This results in a total of seven different models, and

Our motivation is to make the model as simple as possible, providing better understanding of our results and testing which model components are required by the data. These simplifying assumptions can be relaxed in future work. As we show in Appendix C, a strong decrease in $f_{V,cool}$ with radial distance leads to steeper column density profiles and is in tension with the binned measurements presented here (see Figure C1).

We note this is different from the metallicity profile of the warm/hot gas, which varies with radius between Z'=1.0 near the galaxy and Z'=0.3 at r_{CGM} (see Figure 3 in FSM20). Any choice made about the metallicity of the cold gas relative to the hot gas hides an implicit assumption about its theoretical formation mechanism (condensation, accretion, outflows). Choosing a value motivated by observations and constant with radius (i.e., not related to the hot phase) is part of our approach to keep the model simple and phenomenological, and can be revisited in future work.

8.4, 1.2

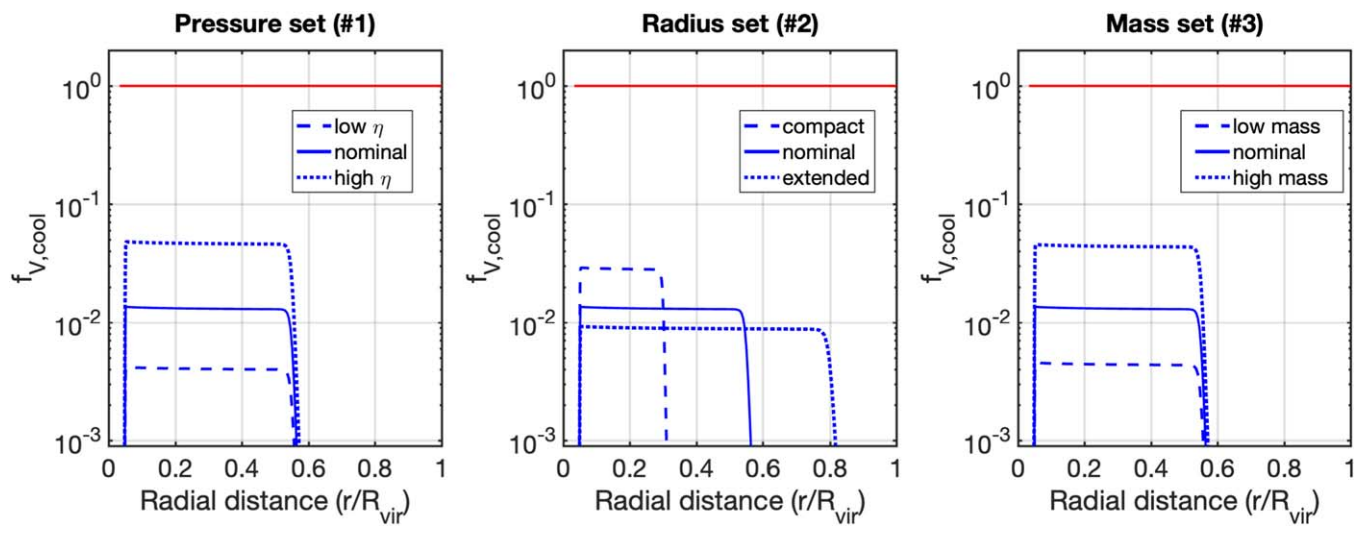


Figure 2. Cool gas volume filling fractions (unity is shown for scale by the red line). In the pressure and radius sets (#1 and #2, left and middle panels), the volume fraction is set to keep the cool gas mass constant between models (see Equation (4)), with $M_{\text{cool}} = 3 \times 10^9 \, M_{\odot}$. In the mass set (#3, right panel) it is set to vary the cool gas mass by a factor of 3 (± 0.5 dex) from the nominal model (see Section 4 for details and Table 1). The model outputs used in this figure are available in machine-readable format.

Trode Troperaes										
			Input Parameters							
	Nominal	Pressure Set (#1, Section 4.1)	Radius Set (#2, Section 4.2)	Mass Set (#3, Section 4.3)	High Mass (Section 5.1)					
$ \eta = \alpha_{\rm cool}/\alpha_{\rm hot} $	3	1, 9	3	3	1,5					
$r_2/R_{ m vir}$	0.55	0.55	0.30, 0.80	0.55	0.55					
$f_{\rm V,cool}/100$	1.30	0.40, 4.6	2.8, 0.90	0.45, 4.4	1.3, 7.8					
			Key Output Properties							
$M_{\rm cool}/10^9 M_{\odot}$	3	3	3	1, 10	10, 10					
$a_{\rm n.c}$	1.67	1.60, 1.74	1.52, 1.76	1.67	1.60, 1.71					

3.2, 1.9

Table 1
Model Properties

their input parameters and main outputs are summarized in Table 1. We plot the gas thermal properties and the volume filling fractions in Figures 1 and 2, respectively. The plots show the profiles for the warm/hot (red) and the cool (blue) phases. We show the full profiles, extending out to $r_{\rm CGM}$, for demonstration, and the thick part of each curve highlights the extent of the nominal model, $r_2 = 0.55 R_{\rm vir}$.

8.1, 0.60

 $n_{0,c}/10^{-4} \,\mathrm{cm}^{-3}$

2.3

As shown in Table 1 and Figure 2, for the models presented in this section, the volume filling fraction is $\approx 0.5\%-5\%$ of the total CGM volume where cool gas is present (and up to 10% in the models discussed in Section 5). These values are similar to the volume filling fraction reported by Ocker et al. (2021) for the MW CGM, $\sim 1\%$, constrained by the amount of scattering measured for fast radio bursts, and significantly higher than the fraction adopted by Vedantham & Phinney (2019), $f_{\rm V,cool} \sim 0.01\%$. In Section 7.1 we discuss how this result can be used to constrain the sizes of cool gas clouds.

The full cool gas density profiles (middle panel of Figure 1) can be approximated as power-law functions of the distance from the halo center, $n_{\rm cool} = n_{0,\rm c} (r/R_{\rm vir})^{-a_{\rm n.c}}$, with $a_{\rm n,c} > 0$, and the fitted parameters are listed in Table 1. For the nominal model, $a_{\rm n,c} = 1.67$, and the full range of slopes for the models presented here is $1.50 \lesssim a_{\rm n,c} \lesssim 1.80$. These approximations are accurate to within 20% of the numerical profiles for models

with $r_2 = 0.55R_{\text{vir}}$, and to 10% and 40% for the compact and extended models in set #2, respectively.

2.3

We now present and discuss each set of models in detail, examining the behavior of gas properties as functions of the model parameters, and comparing the resulting column density profiles, shown in Figure 3 (H I), 4 (C II–C IV), and 5 (Si II–Si IV), to observations. We address the observed and model columns of Mg II separately in Section 4.4 (and Figure 6) since the constraints they provide on the gas properties are similar to those of C II and Si II.

4.1. Set #1: Nonthermal Pressure Support

In this set we vary the amount of nonthermal support in the cool gas and examine three values of η —1, 3, and 9, which we address as low, nominal, and high nonthermal support. The thermal properties for the three models are shown by the dashed, solid, and dotted blue curves, respectively, in Figure 1. The thick part of each curve denotes the range in which the cool gas volume filling fraction is nonzero, out to $r_2 = 0.55$ $R_{\rm vir}$. The left panel of Figure 1 shows $\alpha_{\rm cool} = P_{\rm cool,tot}/P_{\rm cool,th}$ for these models, which varies with radius and is a factor of $\approx 1.5-3$ higher than η .

As shown by Equation (2), for a given total pressure profile of the warm/hot gas, higher η leads to lower cool gas volume

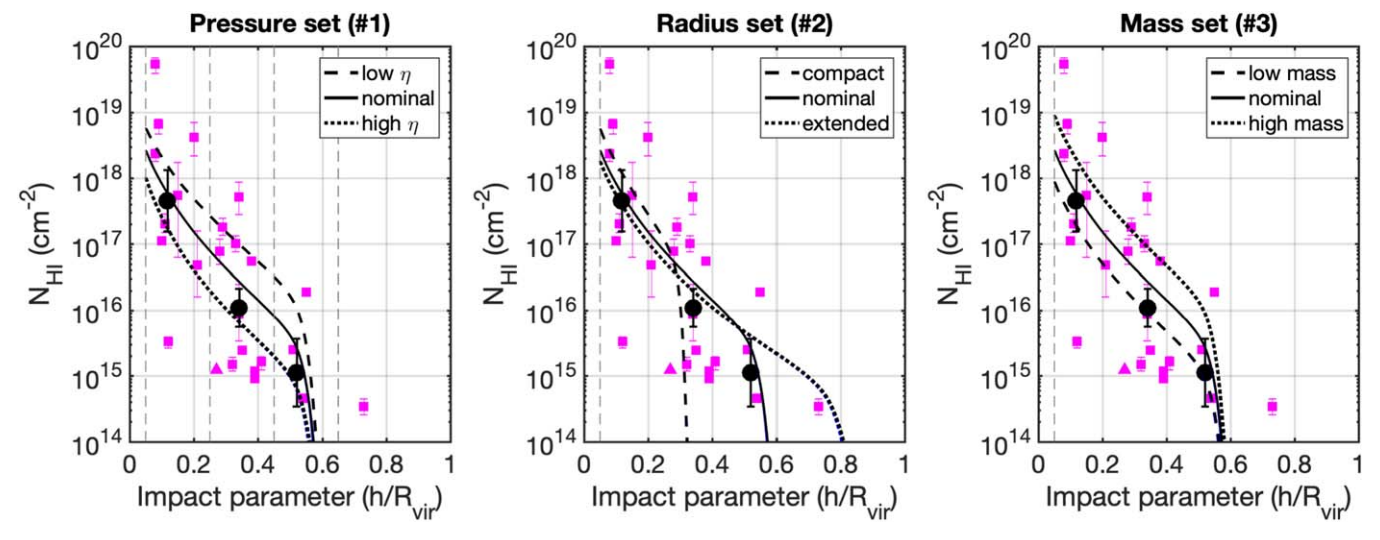


Figure 3. H I column densities—observations, individual, and binned (magenta and black, respectively) and model results for each of the scenarios described in Section 4. Left: in the pressure set (#1), the amount of nonthermal support affects the H I column density through photoionization, with lower densities leading to lower H I fractions. Middle: variation in the gas radial distribution (radius set, #2) affects the shape of the column density profile at large impact parameters. Right: variation in the gas mass through the volume filling fraction (mass set, #3) changes the column density without affecting the gas density and ionization state. The model outputs used in this figure are available in machine-readable format.

densities (middle panel of Figure 1). The volume filling fraction in each model is adjusted to give $M_{\rm cool} = 3.0 \times 10^9 \, M_{\odot}$, leading to higher $f_{\rm V,cool}$ for models with higher η , and these are plotted in the left panel of Figure 2. This is consistent with the results of numerical simulations, finding that gas with higher nonthermal support is more spatially extended (Butsky et al. 2020).

The temperature of the cool phase is set by heating/cooling equilibrium with the MGRF, and it is a function of the gas density and metallicity. For a constant metallicity, lower densities have lower net-cooling rates, leading to higher temperatures. This results in a temperature increase with radius, from $T_{\rm cool} \approx 10^4$ K at small radii (<0.2 $R_{\rm vir}$), to $\approx 2 \times 10^4$ K at $R_{\rm vir}$ (right panel of Figure 1). For the nominal model, extending out to $r_2 = 0.55$ $R_{\rm vir}$, the temperature range is smaller. The variation in gas temperature between models is also small, with a maximal difference of $\approx 25\%$ at $R_{\rm vir}$, compared to the nominal model, and it has a small effect on the ion fractions and column densities.

The gas ionization state changes with gas density and affects the ion fractions, total columns, and their ratios. We provide plots of the ion fractions and volume densities as functions of radius in Appendix B (see Figure B1), and show how the ratio of ion column densities can constrain the amount nonthermal pressure support in Section 5.3. We now describe the behavior of the integrated column densities as functions of η , shown in the left panels of Figure 3 (H I), Figure 4 (C II–C IV, top to bottom), and Figure 5 (Si II–Si IV).

First, for gas at $T \sim 10^4$ K and low densities ($n_{\rm H} < 0.1~{\rm cm}^{-3}$), H I is always removed by radiation. Hence, $N_{\rm H~I}$ (left panel in Figure 3) is higher in the model with low nonthermal support ($\eta = 1$, dashed curve), due to higher gas densities and a lower ionization state. Increasing η leads to lower gas densities and H I fractions and columns (solid and dotted curves). C II and Si II (top-left panels in Figures 4 and 5) behave similarly, with higher (lower) columns for lower

(higher) values of η . Due to the difference in ionization potential between C II and Si II (24.4 and 16.3 eV, respectively), photoionization has a stronger effect on Si II. ¹¹

For C III and Si III (middle left), the effect of photoionization changes at a threshold density of $n_{\rm H,thresh} \sim 5 \times 10^{-4}$ cm⁻³, from forming the ion at higher densities to removing it at $n_{\rm H} < n_{\rm H,thresh}$. In our models, the densities at $r < 0.2~R_{\rm vir}$ are above this threshold, and lower gas densities in that region lead to higher ion fractions. As a result, the C III and Si III columns at small impact parameters are higher in the high- η model (dotted curves). At larger impact parameters, photoionization has a small effect, and the column densities are similar for the different models.

Finally, C IV and Si IV (bottom-left panels) are created by photoionization, and their columns are higher for the high- η model, opposite of the C II and Si II. The C IV and Si IV ion fractions are low at small distances from the galaxy (where the gas densities are higher) and high at larger distances, leading to column density profiles that are relatively flat out to r_2 .

For most of the ions presented here, their column in the warm/hot phase is negligible compared to that in the cool phase (<10% for Si IV, and below 1% for all other ions) and does not appear in our plots. This is not the case for C IV (bottom-left panel in Figure 4), and we plot the contribution from the warm/hot and cool gas with red and blue curves, respectively. In the warm/hot phase, C IV forms mainly at large radii, where the temperature is lower than in the central part of the CGM (see Figure 1) and closer to the optimal value for the ion, with a peak (CIE) fraction at $T\sim10^5$ K.¹² This leads to a flat column density profile, with $N_{\rm C~iv}\sim2\times10^{12}$ cm⁻². The column densities in the cool and hot phases are similar in the low- η model, with $\sim5\times10^{12}$ cm⁻², and in the high- η model, the cool phase dominates, with $N_{\rm C~iv}\approx4-5\times10^{13}$ cm⁻².

¹⁰ This is different from the warm/hot phase, for which FSM20 adopted the polytropic equation of state, resulting in higher temperatures for denser gas, and a temperature profile that decreases at larger distances.

¹¹ The MGRF flux at lower photon energies is higher, and the relative change in ionization parameter for a given change in density is larger.

¹² Since the gas temperature in the warm/hot phase is above the C IV peak temperature, and the ionization parameter at large radii is high, photoionization reduces the C IV ion fraction in the warm/hot phase, instead of increasing it, as it does in the cool phase.

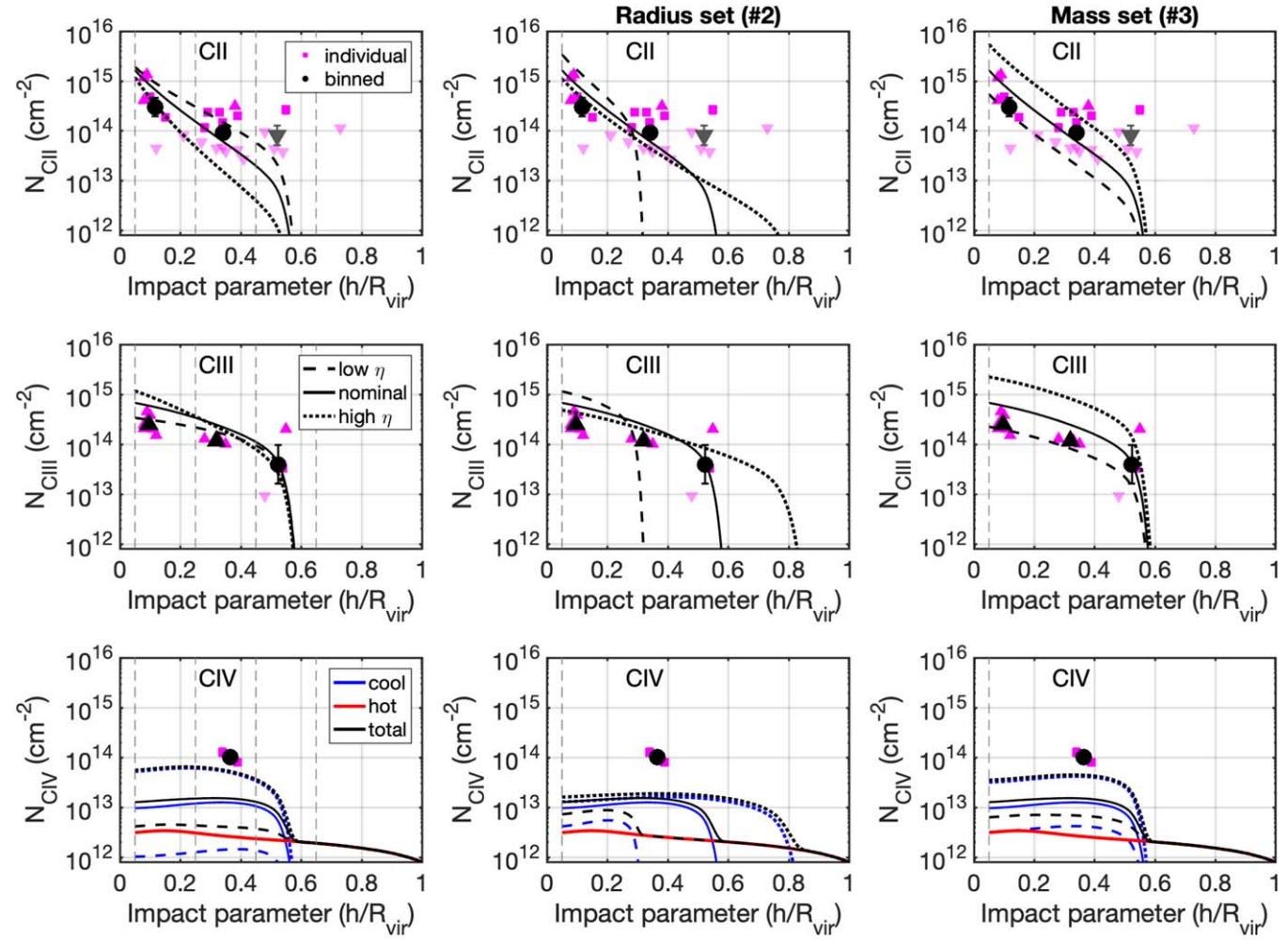


Figure 4. Carbon column densities—observations (markers) and model results for the pressure, radius, and mass sets (left to right), for different ions: C II, C III, and C IV (top to bottom; see Section 4 for details). Individual measured columns are shown by square markers, and lower and upper limits are shown by up-pointing and faded down-pointing triangles, respectively. The vertical dashed lines show the bin boundaries and the innermost radius of the model, $r_1 = 0.05R_{vir}$. For some models, C IV (bottom panels) has a nonnegligible contribution from the warm/hot CGM (red curve). The model outputs used in this figure are available in machine-readable format

We now compare our models to observations. For H I, C II, and Si II, the nominal model is consistent with the binned data, and the range enclosed by the low and high- η models encompasses 50%–75% of the individual measurements and limits. For the intermediate ions, C III and Si III, the three models produce similar column densities. The nominal model is consistent with the C III binned data, and a factor \approx 2–3 higher than the mean Si III column at $h\approx$ 0.35 $R_{\rm vir}$. The detected column densities of the high ions, C IV and Si IV, are underproduced by all three models. However, for Si IV, all three models are consistent with the observed upper limits, which constitute two-thirds of the measurements. The high- η model is a factor of 2–3 lower than the binned Si IV data and the individual detections at $h \lesssim 0.4~R_{\rm vir}$, with column densities of \sim 3–8 \times 10¹³ cm⁻². This model also predicts a total C IVcolumn of \sim 7 \times 10¹³ cm⁻², within a factor of \lesssim 2 of the measured values at $h\approx$ 0.35 $R_{\rm vir}$, with $N_{\rm C~iv}\sim$ 10¹⁴ cm⁻². We discuss possible solutions for this tension in Section 5.

4.2. Set #2: Radial Distribution

In this set, we vary the outer radial boundary of the cool gas spatial distribution, and examine models with $r_2 = 0.30$, 0.55,

and $0.80\,R_{\rm vir}$, which we address as compact, nominal, and extended, respectively. The gas thermal properties do not vary with r_2 and are plotted as functions of radius by the solid curves in Figure 1. The volume filling fraction in each model is adjusted to give a gas mass of $M_{\rm cool}=3\times10^9\,M_{\odot}$ (identical to set #1), and they are plotted in the middle panel of Figure 2. The solid curve in each panel shows the nominal model, and the dashed and dotted lines show the compact and extended distributions, respectively.

The middle panel of Figure 3 shows the HI column densities for these three models, and carbon and silicon ions are shown in the middle column panels of Figures 4 and 5, respectively. For a given density profile, the shape and normalization of the column density profiles are determined by two factors: (i) the mean gas density, varying with the gas radial extent, sampling different parts of the full density profile, and (ii) the volume filling fraction, which for a given total gas mass is lower for more extended distributions (see middle panel of Figure 2). For example, the low ions—CII, SiII (top-middle panels of Figures 4 and 5), and HI—form mostly in the inner region of the halo (see also Figure B1 in Appendix B), resulting in steep profiles with impact parameter. In the compact distribution, more mass is concentrated at these radii, leading to

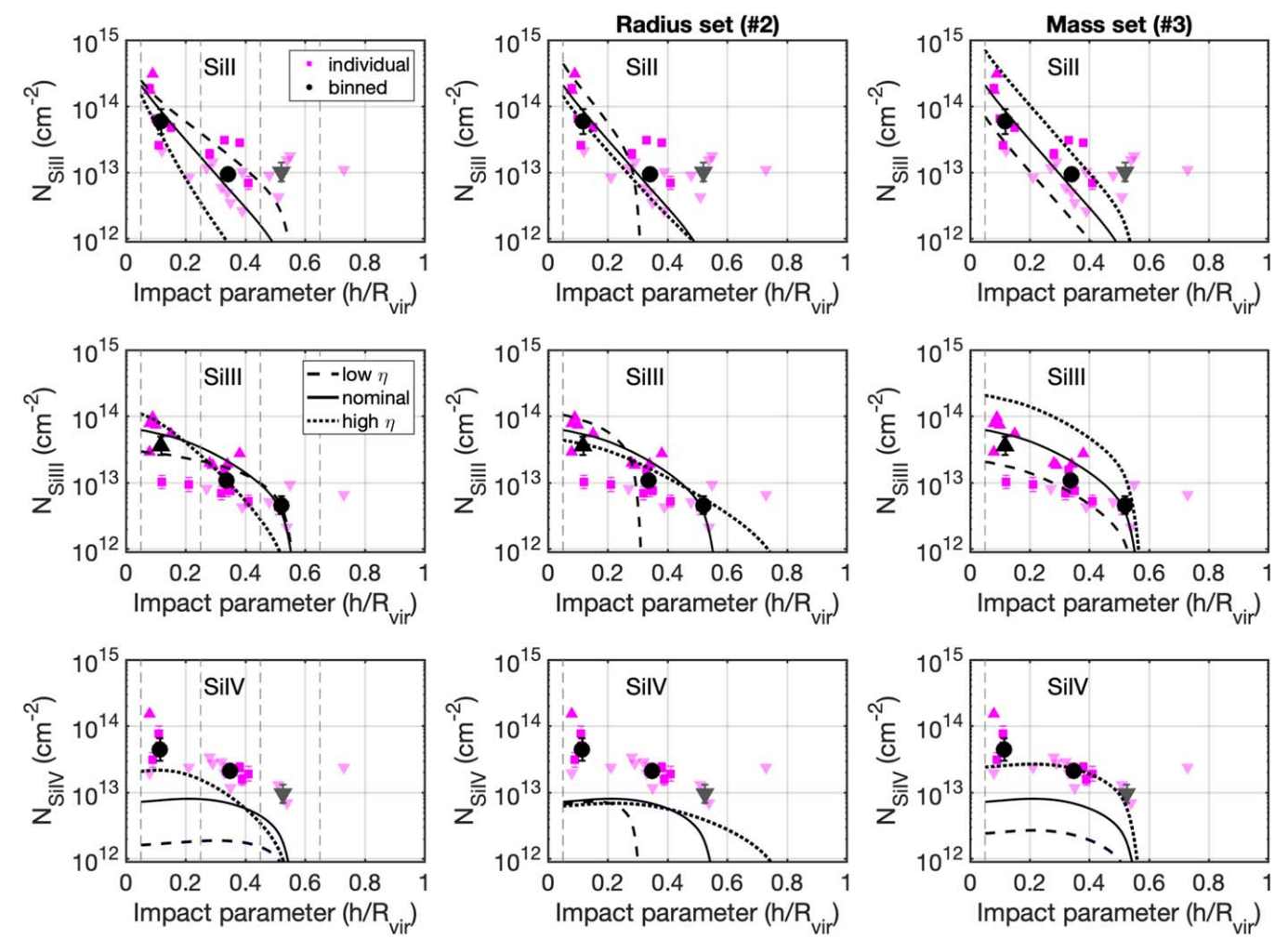


Figure 5. Silicon column densities—same as Figure 4, for Si II, Si III, and Si IV (see Section 4 for details). The model outputs used in this figure are available in machine-readable format.

column densities that are higher by a factor of 2–3 at small impact parameters, compared to the nominal model. The intermediate ions—C III and Si III (center panels)—form at larger distances and have flatter profiles. The high ions—C IV and Si IV (bottom-middle panels)—are formed mainly in low-density gas, residing at large distances from the halo center. This results in flat column density profiles out to r_2 , and lower columns in the more compact distributions.

As described in Section 4.1, the total C IV column density has a nonnegligible contribution from the warm/hot gas, with $N_{\text{C IV,hot}} \sim 1-2 \times 10^{12} \text{ cm}^{-2}$ (shown by the red curve in the bottom-middle panel of Figure 4). The total C IV column density (black curve) is divided equally between the cool and warm/hot phases in the compact model, and dominated by the cool phase in the extended model. For the nominal model, the C IV column density in the cool component at $h < 0.5R_{\text{vir}}$ is higher by a factor of 3–4 than in the warm/hot component.

Compared to observations, the nominal and extended models are similarly consistent with the mean columns of low and intermediate ions, up to a factor of \sim 2. At impact parameters where the two models differ significantly, $h \gtrsim 0.5~R_{\rm vir}$, the C II and Si II observations provide mostly upper limits, and both models are allowed by the data. Future measurements at these large radii may allow us to better constrain the cool gas distribution (see also Wilde et al. 2021; Tchernyshyov et al. 2022

for CGM² data). The compact model overproduces (underproduces) the binned data of the low and intermediate ions at small (large) impact parameters, below (above) $h \approx 0.3~R_{\rm vir}$, and one can argue that it can be ruled out for the average profile. However, the H I measurements show a cluster of data at $0.3 < h/R_{\rm vir} < 0.6$, with $N_{\rm H~I} \sim 10^{15}~{\rm cm}^{-2}$, which are enclosed by the compact and extended model curves. This suggests that these low H I columns may be indicative of the spatial extent of the cool gas distribution in individual objects.

The observed column densities of the high ions, C IV and Si IV, are underproduced by all three models, similar to the result of the pressure set. The Si IV detections at $h \sim 0.35~R_{\rm vir}$, with column densities of $\sim 2 \times 10^{13}~{\rm cm}^{-2}$, are higher than the models by a factor of $\gtrsim 4-5$. The C IV measurements at similar impact parameters, with $N_{\rm C~iv} \sim 10^{14}~{\rm cm}^{-2}$, are about an order of magnitude higher than the total model columns.

Finally, we consider a variation in the inner boundary of the cool gas distribution. For the models presented here, we use $r_1 = 0.05R_{\rm vir}$. Adopting a value of $r_1 \sim 0.2~R_{\rm vir}$, for example, for the nominal or extended models, produces a constant column density at $h < r_1$. For $M_{\rm cool} = 3 \times 10^9~M_{\odot}$, this results in low columns, inconsistent with the high measurements and lower limits at these impact parameters, and increasing $M_{\rm cool}$ overshoots the low ion columns at larger h. Furthermore, the lack of cool gas in the vicinity of the galaxy, while not

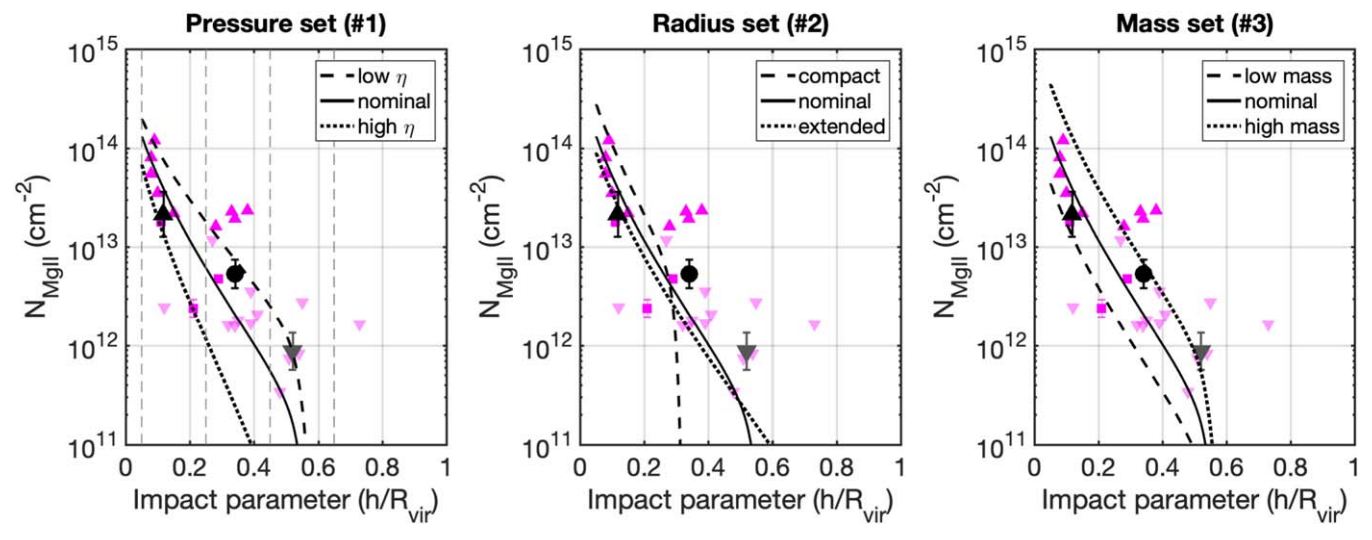


Figure 6. Mg II column densities—observations and model results (see Sections 4 and 4.4 for details). The model outputs used in this figure are available in machine-readable format.

impossible, may be an unusual scenario. For example, in the MW, many of the high-velocity clouds (HVCs), detected in 21 cm, reside relatively close to the Galactic disk, at d < 20 kpc (Putman et al. 2012).

4.3. Set #3: Gas Mass

In this set of models we vary the total gas mass in the cool component, by changing its volume filling fraction, $f_{\rm V,cool}$ (see Equation (4)), and these are plotted in the right panel of Figure 2. The masses of these models are 1, 3, and $10 \times 10^9 \, M_\odot$, and they are shown by the dashed, solid, and dotted curves, respectively. These masses constitute ~1.8% (8.3%), 5.5% (25%), and 18% (83%) of the warm/hot CGM mass in the FSM20 fiducial model inside $R_{\rm vir}(r_2)$, and see Figure 10). The gas volume density profile (middle panel in Figure 1) does not change between models, and the ion column densities are linear with $f_{\rm V,cool}$ (see Equations (5)–(6)). We now show that the range of columns produced by these models is consistent with a large fraction of the observations.

The H I column density profiles are shown in the right panel of Figure 3 and encompass half of the individual measurements. Data points outside the range predicted by the models are either low or very high columns. Sight lines with low column densities, $N_{\rm H\,I} \sim 1-4 \times 10^{15}$ cm⁻², may probe the outer boundaries of the cool gas distributions in the CGM, as suggested in Section 4.2, or belong to objects that are gasdeficient. The high columns, $N_{\rm H\,I} \gtrsim 10^{18}$ cm⁻², can be explained by models with higher gas density and higher mass cool phase (see Section 5.1), or by a large/high-density structure that intersects the line of sight (similar to the Magellanic Stream in the MW, for example.).

The metal ion columns are shown in the right column of Figures 4 and 5, and the range predicted by this set of models is consistent with >3/4 of the individual data points for the low and intermediate ions. The top-right panels show the C II and Si II column densities, and the models are consistent with 20/25 data points for each ion. The intermediate ions (middle right) in the model are also consistent with most of the measurements—the Si III columns are consistent with 19/24 of the data points, and the C III columns are at or above the observed lower limits, constituting 10/12 of the measurements.

For C IV and Si IV (bottom right), the high-mass model columns are below the binned data, by a factor of $\lesssim 3$.

4.4. Mg II

Mg II is an ion that is often measured in the CGM (Steidel & Sargent 1992; Churchill et al. 2000; Rigby et al. 2002). The doublet wavelength, at $\lambda=2796,\,2803A$, is close to the optical and can be probed from the ground at low to high redshifts (Charlton & Churchill 1998; Prochter et al. 2006; Chen et al. 2010; Kacprzak et al. 2011; Matejek & Simcoe 2012; Evans et al. 2013; Nielsen et al. 2013). The high signal-to-noise ratio and complementary information provided by ground-based observations enable relating the properties of Mg II absorbers to galaxy dynamics and morphology (Kacprzak et al. 2010; Bordoloi et al. 2011, 2014; Ho et al. 2017; Ho & Martin 2020; Tejos et al. 2021).

Figure 6 shows the Mg II column densities measured for the COS-Halos sight lines with Keck/HIRES (Werk et al. 2013) and the column densities for the models described in Sections 4.1–4.3. The Mg II ionization potential is 15.0 eV, close to that of Si II (16.3 eV), leading to similar column density profile shapes for the two ions in our models, and the Mg II profiles are slightly steeper. The solar abundance of magnesium is similar to that of silicon $(A_{\rm Mg}/A_{\rm Si}\approx 1.25)$, and the absolute columns for the two ions are also similar.

The overall scatter in the observations is similar to that seen in C II and Si II, and maybe slightly more bimodal, with most of the reported measurements being upper or lower limits. Similar to the results presented in Section 4.2, the compact model underpredicts the column in the second radial bin. The models in the pressure and mass sets (#1 and #3) are consistent with a large fraction of the individual measurements or limits—17/25 for η variation, and 19/25 for variation in $M_{\rm cool}$.

To summarize this section, we presented a nominal model that is consistent with the binned measurements of low and intermediate ion column densities. We also explored how variation of each model parameter affects the cool gas properties and resulting column densities. We showed that models with $1 < \eta < 9$ ($2 \lesssim \alpha_{\rm cool} \lesssim 20$) produce column densities that are consistent with the binned measurements of the low and intermediate ions, and with $\approx 2/3$ of the individual

detections and limits for these ions. Models with cool gas masses between 10^9 and $10^{10}\,M_\odot$ encompass $\approx 3/4$ of the individual measurements for the low and intermediate ions. Models with variation in the spatial extent of the distribution suggest that the cool gas of a typical galaxy extends to $\approx 0.5-0.6\,R_{\rm vir}$. However, low HI columns in individual objects may be indicative of outer boundaries between 0.3 and $0.8\,R_{\rm vir}$. The model parameter combinations presented here underpredict the column densities of the high metal ions, C IV and Si IV, by factors of 2–10. Furthermore, about 20% of the observed objects in our sample have HI columns higher than predicted by the models. In the next section we present models with variation in more than one parameter from the nominal model, and show these can reproduce the measured high and low column densities.

5. Model Demonstration: Advanced

We now explore models that can produce columns lying beyond the typical scatter given by the models in Section 4. First, in Section 5.1, we explore cool gas models that combine variation in two parameters from the nominal values. We show that a high mass and low- η combination gives high H I columns, and the high-mass and high- η model reproduces the measured columns of high ions, C IV and Si IV. Then, in Section 5.2 we address a scenario where the latter are produced in warm, intermediate-temperature gas. We present the results of these models in Figure 7.

5.1. High Cool Gas Mass

In Section 4, we showed how variations in the model main parameters—nonthermal support, radial extent, and gas mass—affect the ion column density profiles. We addressed each parameter separately to better understand its effect, both qualitatively and quantitatively. For example, the effect of nonthermal support on the ion columns varies between the low and high ions—increasing η reduces the local gas density, increases the gas ionization parameter, and leads to a higher ratio of the high to low ion column densities (see Section 4.1 and left panels of Figures 3–6). Varying the cool gas mass through the gas volume filling fraction, on the other hand, affects all columns in the same way, since $N_{\rm ion} \propto f_{\rm V,cool}$ (Section 4.3, right panels).

We now show that models with higher mass, $M_{\rm cool} = 10^{10} \, M_{\odot}$, can reproduce either the high H I or Si IV (and C IV) observed columns, depending on the gas ionization state, set by the value of η . We examine two specific models, one with $\eta = 1$, and the other with $\eta = 5$, both with the nominal spatial extent, $r_2 = 0.55 \, R_{\rm vir}$, and metallicity, Z' = 0.3. We show some results of the two models in the top panels of Figure 7—the gas densities (left), the H I columns (middle), and the Si IV columns (right). We also plot the outputs of the nominal model from Section 4, for comparison. The main inputs and outputs of the two models are also listed in Table 1.

The model with $\eta=1$ (dashed curves) has high volume gas densities (top-left panel), with a profile identical to the low- η model in Section 4.1. This increase is enough to give the higher gas mass, and the volume filling fraction is similar to the nominal model, with $f_{V,cool}=1.3\%$. The higher density gas is less ionized, compared to nominal, and has higher H I fractions. The combination of higher gas densities and higher H I fractions leads to an increase by a factor of ~ 10 in the H I column densities (top middle), and these are comparable to

the highest measured columns. The Si IV ion fractions, on the other hand, are lower than in the nominal model, canceling out the increase in $n_{\rm H}$, and the resulting columns are similar to the nominal (top right).

The model with $\eta = 5$ (dotted curves) has lower gas densities, and to produce the same gas mass requires a higher volume filling fraction, $f_{\rm V,cool} = 7.8\%$. The gas is more ionized, resulting in lower H I fractions, but the increase in $f_{\rm V,cool}$ offsets the decrease in gas density and ion fraction, and the H I columns are similar to those in the nominal model. The Si IV fractions are higher, and the resulting column densities are consistent with the binned data, and the individual measurements at ≈ 0.2 and ≈ 0.4 $R_{\rm vir}$. This model also reproduces the observed C IV columns at ≈ 0.4 $R_{\rm vir}$ (not plotted here; see attached data files).

These results provide a general prediction from our model for the behavior of low and high ions in individual objects. For example, sight lines with high H I columns should have nominal columns of high ions (similar to nominal), and vice versa—sight lines with high Si IV columns should have nominal H I columns. The modeling of individual objects is beyond the scope of this paper, to be pursued in a follow-up study.

Finally, a combination of low $M_{\rm cool}$ with low η will produce typical H I columns and very low columns for high ions, and low $M_{\rm cool}$ with high η will give very low H I and typical columns for high ions. These may also be interesting for individual objects or future observations with strong upper limits.

5.2. Intermediate-temperature Gas

We now consider a second option, in which the high ions columns are formed in gas with a temperature distribution between that of the warm/hot and the cool phases. Possible scenarios for such models include gas that is cooling from the hot phase (Heckman et al. 2002; Qu & Bregman 2018a), or mixing gas at the boundaries of cool clouds (Ji et al. 2019; Fielding et al. 2020; Gronke & Oh 2020; Tan et al. 2021).

To test this scenario, we model an intermediate-temperature (hereafter IT) phase with a flat probability distribution, occupying the range between the temperatures of the warm/hot and the cool phases, $T_{\rm hot}$ and $T_{\rm cool}$, at a given radius. We adopt a distribution function given by $p(T) \propto T^{-1}$, flat in logarithmic temperature bins, and verify that adopting $p(T) = {\rm const.}$, flat in linear bins, gives similar results. We assume that the gas in this phase is isobaric, and the gas mass is then given by

$$M_{\rm IT} = 4\pi \int_{r_1}^{r_2} \bar{m}(r) f_{\rm V,IT}(r) dr \int_{T_{\rm cool}}^{T_{\rm hot}} p(T) n_{\rm IT}(T) dT,$$
 (7)

and the column density for a given ion can be written as

$$N_{\text{ion}}(h) = \int_{s} f_{\text{V,IT}}(r) A_{X} Z'(r) \int_{T_{\text{cool}}}^{T_{\text{hot}}} p(T) n_{\text{IT}}(T) f_{\text{ion}}(T) dT ds,$$
(8)

where $f_{\rm V,TT}$ is the volume filling fraction of IT gas, taken to be constant with radius. We adopt the nominal extent and metallicity of the cool gas for the IT phase, $r_2 = 0.55 \, R_{\rm vir}$ and Z' = 0.3, and vary the gas mass of the latter through $f_{\rm V,IT}$, to reproduce the observed C IV and Si IV column densities.

¹³ In general, the metallicity of the intermediate-temperature phase is related to the origin of this phase (cooling, mixing, etc). Here we assume for simplicity that the metallicity of the intermediate phase is constant and equal to that of the cool gas; a more detailed treatment can be undertaken in a future study.

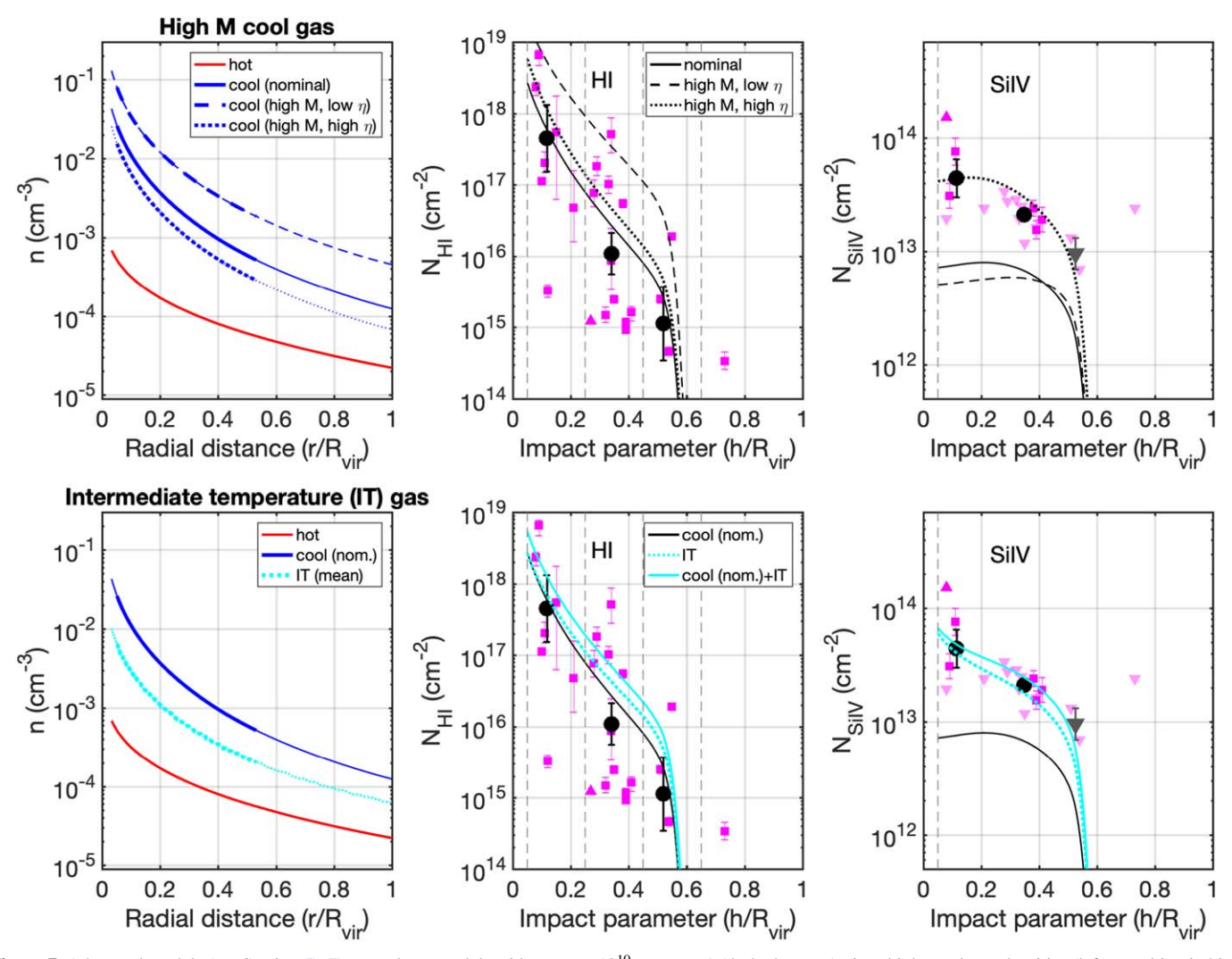


Figure 7. Advanced models (see Section 5). Top: cool gas models with $M_{\rm cool} = 10^{10} \, M_{\odot}$, $\eta = 1$ (dashed curves) gives higher volume densities (left), resulting in high H I columns (middle panel) and Si IV columns similar to the nominal model (right). $\eta = 5$ (dotted) produces highly ionized gas, with high Si IV, similar to the measured values, and nominal H I columns. Bottom: intermediate-temperature gas (cyan dotted curves) with $M = 1.5 \times 10^{10} \, M_{\odot}$ and $f_{\rm V} \approx 40\%$ can reproduce the measured Si IV column densities. Since this is a separate phase, the columns are added to those in the cool phase, and the total columns are shown by the cyan solid curves. The model outputs used in this figure are available in machine-readable format.

The dotted curves in the bottom panels of Figure 7 show a model with $M_{\rm IT}\approx 1.3\times 10^{10}\,M_{\odot}$. The mass-weighted mean density (dotted cyan curve, bottom left) is a factor of $\approx 2-3$ lower than the cool gas density in the nominal model (solid blue), and similar to that of the cool gas model with $\eta=5$ presented in Section 5.1 (dotted curves, top panels). The column densities for H I (bottom middle) are also similar to the columns in the nominal model for the cool gas, and the total columns (cool+IT, solid curve) are a factor of ≈ 2 higher. Similarly, the column densities of low metal ions (C II, Si II, Mg II) in IT gas are a factor of 1–2 higher than those in the cool gas. ¹⁴ The total Si IV column densities (bottom-right panel) and the C IV (not shown) are dominated by the IT component.

To match the observed high ion columns, the model requires the IT phase to have a volume filling fraction of $\sim\!40\%$, significantly larger than that of the cool gas, both in the nominal and high mass models, with $f_{\rm V,cool} \approx 1\%$ and $\approx\!10\%$, respectively. The resulting picture is different from simulation results that find thin mixing layers occupying a small fraction

of the total volume (Ji et al. 2019; Fielding et al. 2020; Gronke & Oh 2020; Ji et al. 2020; Tan & Oh 2021; Tan et al. 2021; Gronke et al. 2022). With a high $f_{\rm V,IT}$, our result may be more consistent with IT gas that cools from the warm/hot phase. For cooling gas, models usually assume that the gas probability distribution is proportional to its cooling time, resulting in small amounts of gas at $T \sim 2 \times 10^5$ K, which has high cooling efficiency (Heckman et al. 2002; Qu & Bregman 2018a, 2018b). However, it is gas at these temperatures that has high Si IV and C IV fractions in CIE. Figure 8 shows the cumulative gas mass distribution as a function of temperature for the IT component in our model. The half mass temperature, marked by the black square, is $\approx 9 \times 10^4$ K, and 80% of the gas mass is between 2×10^4 K and 4×10^5 K (shown by circles).

Our finding that high volume fractions are needed to reproduce the observed C IV and Si IV column densities is similar to that of Gnat & Sternberg (2004), who found that a large number of boundary layers is needed to reproduce the measured O VI columns. We calculated how much O VI forms in the IT component, and found that the O VI column density profile has a similar shape to that of the Si IV, decreasing from

¹⁴ These columns are not plotted here but are provided in the data files.

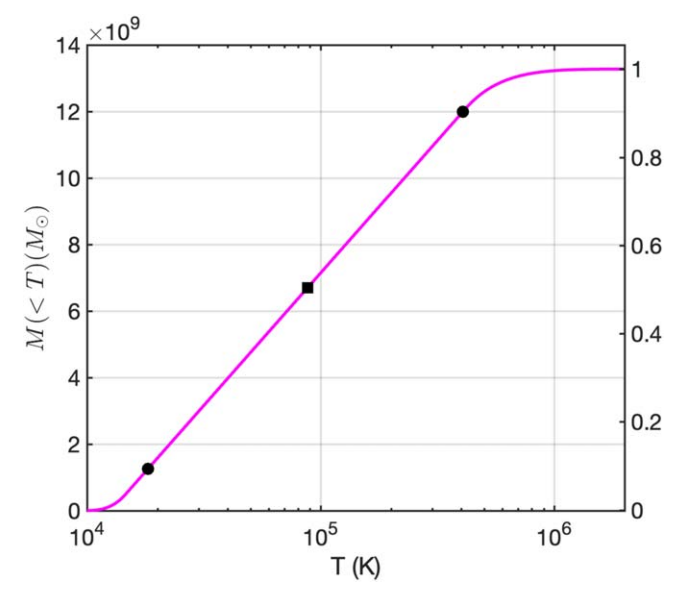


Figure 8. The cumulative gas mass distribution as a function of temperature for the IT component (see Section 5.2 for details). The labels on the left *y*-axis show the mass in solar masses, and on the right show normalized to the total, $M_{\rm IT} = 1.3 \times 10^{10} \, M_{\odot}$. The circles mark 10% and 90% of the total mass, and the square shows the half mass temperature, $T \approx 9 \times 10^4 \, {\rm K}$.

 $\approx \! 10^{14} \; \mathrm{cm}^{-2}$ in the inner part of the CGM, at $h/R_{\mathrm{vir}} = 0.05$, to $\approx \! 10^{13} \; \mathrm{cm}^{-2}$ at $h/R_{\mathrm{vir}} \approx 0.5$. For comparison, the fiducial warm/hot gas model in FSM20 reproduces the observed O VI columns, $\approx \! 4 \times 10^{14} \; \mathrm{cm}^{-2}$, approximately constant with impact parameter. Thus, while the O VI originating in the IT phase is not negligible at small impact parameters, it alone cannot reproduce the high measured columns at larger h/R_{vir} . In Section 7.1 we estimate the cloud sizes for the cool and IT phases and the number of clouds along the line of sight.

We presented the column densities forming in the cool and IT gas separately, allowing us to address different physical scenarios. In the mixing layers picture, for example, the IT gas is an additional component to the cool phase. Our calculations show that the IT component alone can account for the column densities for the low and intermediate ions, suggesting the amount of cool gas may be negligible ($f_{V,cool} < < 1\%$). However, since gas at intermediate temperatures has a high cooling efficiency, a significant heating rate is needed to keep it from cooling to the equilibrium temperature set by the MGRF. For the parameters presented here, the integrated cooling rate for the IT component is $\sim 10^{41}$ erg s⁻¹, similar to that of the entire warm/hot CGM in the FSM20 fiducial model.

Finally, we note these results depend on the assumed metallicity for the IT phase. Increasing the metallicity by a factor of 2 (to Z'=0.6) and keeping the same C IV columns allows us to reduce $M_{\rm IT}$, $f_{\rm V,IT}$, and $N_{\rm H\,I}$ in this phase by a factor of 2, resulting in a better agreement with the measured H I columns. However, the columns of low and intermediate metal ions and the volume filling fraction ($\approx 20\%$) will still be high compared to observations and mixing layers simulations, respectively. As noted above, the metallicity of the intermediate phase depends on the origin of the cool gas and on the small-scale physics in the boundary mixing layers, and we leave a more detailed treatment of this issue to future studies.

5.3. Estimating Gas Properties

In Sections 4 and 5.1 we presented models with specific parameter combinations and showed that by varying the nonthermal support and gas mass in the cool phase, our model framework allows us to reproduce the mean observed column densities, the scatter in the data, and the high columns measured in some objects. We now perform a brief exploration of the model parameter space, and present outputs for a continuous variation of η and h. We demonstrate how these can be used to easily relate the measured column densities to the properties of the cool CGM. As noted earlier, we leave the full modeling of individual lines of sight to a separate study.

First, since in this work the gas metallicity Z' and volume filling fraction $f_{\rm V,cool}$ are constant as functions of radius, the metal column density ratios are independent of the assumed values for these parameters. For two ions of the same element, the ratio is also independent of the elemental abundance, and is only a function of the impact parameter and the amount of nonthermal support. As an example, in the left panel in Figure 9 we plot the $N_{\rm C~II}/N_{\rm C~III}$ ratio in this 2D parameter space, for models with $r_2 = 0.55 r_{\rm CGM}$, and $M_{\rm cool} = 3 \times 10^9 M_{\odot}$. The ratio of the measured columns for a given sight line allows to constrain the nonthermal support in the cool gas.

Second, the ratio of a given metal ion to HI columns scales linearly with metallicity, and independent of the volume filling fraction. The middle panel plots the C II/HI column density ratio in our model, for a metallicity of Z'=0.3, and for the Asplund et al. (2009) solar carbon abundance ($A_C=2.7\times10^{-4}$). For an observed sight line, the metallicity is given by the ratio of the measured C II/HI to the ratio in the plot, at the value of η inferred in the previous step. The C II and HI fractions behave similarly with ionization parameter (i.e., gas density, see Figures 3–4), and the overall variation in C II/HI ratio with impact parameter and nonthermal support is relatively small.

Finally, the total H I column scales linearly with the volume filling fraction and it is plotted in the right panel of Figure 9 for $f_{\rm V,cool}=1\%$. Similar to the metallicity, $f_{\rm V,cool}$ is given by the ratio of the measured H I column to the plotted value at a known η . At a given impact parameter, the H I column depends strongly on η , scaling as $\propto \eta^{-2.4}$. This strong dependence is a result of two factors—lower gas densities lead to lower total hydrogen densities, and smaller neutral fractions, due to the gas higher ionization state.

The nonthermal support in the cool gas and its volume filling fraction give M_{cool} . Inserting Equation (2) into Equation (4), the mass can be written as

$$M_{\rm cool} = \frac{f_{\rm V,cool}}{\eta} \int_{r_1}^{r_2} \frac{T_{\rm hot}}{T_{\rm cool}} dM_{\rm hot}. \tag{9}$$

In this study, we assume the fiducial FSM20 gas distribution for the warm/hot CGM, and $T_{\rm hot}(r)$ is the same for all of the models we examine (but see Section 6.1 here). However, as shown in Section 4, the temperature of the cool component depends (weakly) on the gas density, which depends on the value of η . As a result, the gas mass deviates slightly from a linear function of η , and approximating it as a power law we

¹⁵ If the model is used to reproduce only the metal column densities, without a measured hydrogen column, the gas metallicity and volume filling factor are degenerate, and only their product can be constrained.

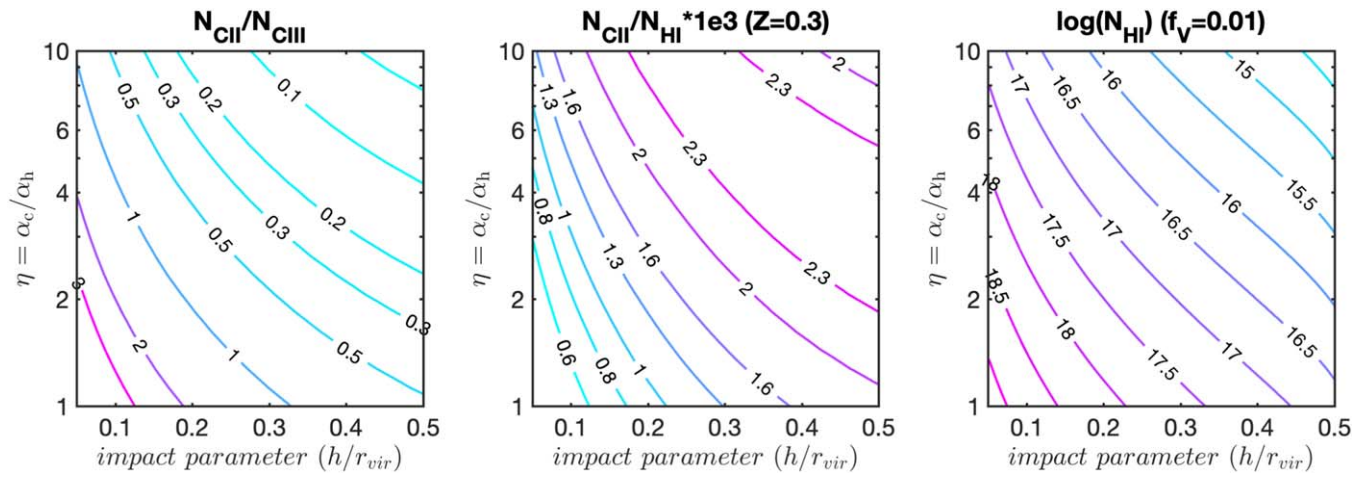


Figure 9. Estimating the cool gas parameters in individual lines of sight, using a model with $r_2 = 0.55 R_{vir}$ (see Section 5.3 for details). Left: the C II/C III column density ratio constrains η , the amount of nonthermal support. Middle: the C II/H I column density ratio allows to infer the gas metallicity. Right: $N_{\rm H~I}$ is a proxy for the cool gas volume filling fraction and mass (see also Figure 10).

can write

$$M_{\rm cool} \approx 2.3 \times 10^9 \times \left(\frac{\eta}{3}\right)^{-1.15} \left(\frac{f_{\rm V,cool}}{10^{-2}}\right) M_{\odot}.$$
 (10)

We plot the total mass of cool gas, without approximation, in Figure 10 for $r_2 = 0.55~R_{\rm vir}$. The individual markers show the models presented in Section 4 (blue circles) and in Section 5.1 (black squares). The thick red contours show the masses of warm/hot gas in the FSM20 fiducial model in the spherical volume enclosed by r_2 (dashed) and $R_{\rm vir}$ (solid), with $M_{\rm hot} = 1.2 \times 10^{10}$ and $4.6 \times 10^{10} \, M_{\odot}$, respectively.

6. Model Uncertainties

We now address some of the assumptions of our model and the uncertainties of its components, and discuss their implications for the results presented in this work.

6.1. Underlying Hot Gas Distribution

The cool gas density in our model is set by the pressure profile of the warm/hot, volume-filling phase, and any profile for the latter can be used within our framework. In this work, we adopted the distribution from the FSM20 fiducial model, and we now discuss how our main conclusions are affected by using a different pressure profile for the ambient medium. To address this, we look at the warm/hot gas density and pressure profiles from Faerman et al. (2022), who considered two additional models with different amounts of nonthermal support—one with only thermal support in the warm/hot gas ($\alpha_{\text{hot}} = 1$), and the second dominated by nonthermal support ($\alpha_{\text{hot}} = 3$, and see their Figure 6 for the gas thermal properties). We repeated our calculations for the cool gas nominal model parameters with these distributions, and we now describe the main findings of this analysis, also summarized in Table 2.

Before addressing the results, we note two points: (i) Faerman et al. (2022) showed that models with low or high nonthermal pressure under- or overproduce, respectively, the measured OVI columns. This supports our choice of the FSM20 fiducial warm/hot gas parameters for this work, and the discussion here is mostly qualitative, to gain a better

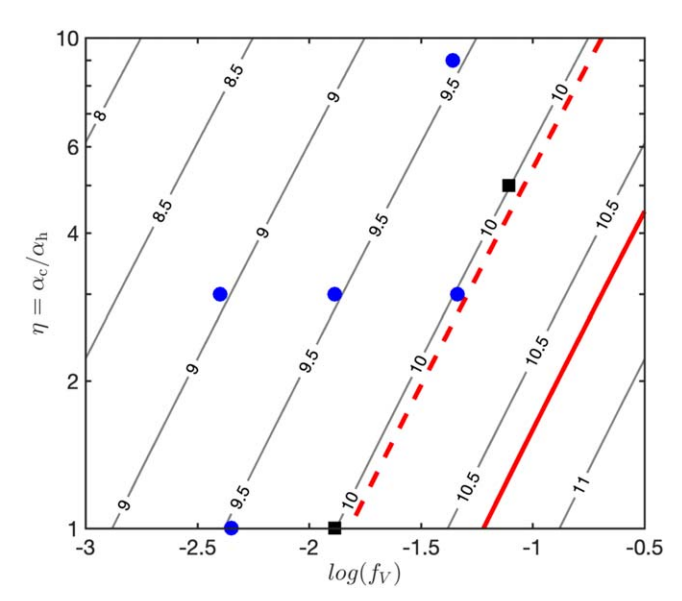


Figure 10. The cool gas mass as a function of the nonthermal support and volume filling fraction, for $r_2=0.55\,R_{\rm vir}$ (see Section 5.3 for details). The markers show the individual parameter combinations adopted for the basic models discussed in Section 4 (blue circles), and the advanced models in Section 5.1 (black squares). The thick red contours indicates the warm/hot gas mass inside the spherical volume enclosed by r_2 (dashed) and inside $R_{\rm vir}$ (solid), with $M_{\rm hot}=1.2\times10^{10}$ and $4.6\times10^{10}\,M_{\odot}$, respectively.

 $\begin{tabular}{ll} \begin{tabular}{ll} Table~2\\ \begin{tabular}{ll} Variation~in~Nonthermal~Support~in~the~Warm/Hot~Phase\\ \end{tabular}$

	Thermal $(\alpha_{hot} \approx 1)$	Nonthermal ($\alpha_{hot} \approx 3$)
P _{th,hot} —profile shape	steeper	flatter
$P_{\rm th,hot}(r < 0.6 R_{\rm vir})$	higher	lower
(a) fixed η	higher $n_{\rm cool}$	lower $n_{\rm cool}$
(b) fixed α_{cool}	similar $n_{\rm cool}$	similar $n_{\rm cool}$

understanding of the cool gas model. (ii) The results presented here are valid at a given gas mass and boundary temperature in the warm/hot phase, and an exploration of the parameter space for a model with warm/hot and cool gas may be the focus of a future study.

To demonstrate the effect the warm/hot gas distribution has on the cool gas, we use Equation (2):

$$n_{\rm cool} = \frac{P_{\rm th,hot}/k_{\rm B}}{\eta T_{\rm cool}} = \frac{\alpha_{\rm hot}}{\alpha_{\rm cool}} \frac{P_{\rm th,hot}/k_{\rm B}}{T_{\rm cool}}.$$
 (11)

We address how variation in $\alpha_{\rm hot}$, the amount of nonthermal support in the warm/hot gas affects its pressure profile, and then how this affects the cool gas properties for two subcases: (a) fixing the value of η to that of our nominal model, i.e., a constant ratio between the nonthermal pressures in the warm/hot and cool phases, and (b) fixing $\alpha_{\rm cool}$ to the values in the nominal model, i.e., a given ratio of nonthermal to thermal pressure in the cool phase. These two cases may correspond to (a) cool gas forming by condensation from the warm/hot phase with nonthermal pressure from magnetic fields, for example, and (b) cool gas originating from "external" sources, such as outflows, dwarf galaxies, or IGM accretion.

First, for warm/hot gas with only thermal support ($\alpha_{\rm hot} \approx 1$), at a given total gas mass and fixed thermal temperature at the outer boundary, the warm/hot gas temperature and density profiles are steeper than in the fiducial model, leading to a steeper thermal pressure profile, and higher pressures at radii <0.6 $R_{\rm vir}$. For a fixed value of η , these higher pressures lead to higher cool gas densities. For a fixed value of $\alpha_{\rm cool}$, the lower $\alpha_{\rm hot}$ increases η , negates the effect of higher $P_{\rm th,hot}$, and leads to cool gas densities similar to the nominal model.

Second, for warm/hot gas with higher nonthermal support $(\alpha_{\rm hot} \approx 3)$, the temperature and density profiles are flatter than the fiducial FSM20 distributions, leading to lower pressures at $r < 0.6~R_{\rm vir}$. For a fixed η , lower $P_{\rm th,hot}$ lead to lower cool gas densities. For a fixed $\alpha_{\rm cool}$, the result is lower η , and cool gas densities that are similar to the nominal model.

To summarize our results qualitatively, we find that for a given value of η , lower (higher) nonthermal support in the warm/hot phase leads to higher (lower) ambient gas pressure at $r < 0.6~R_{\rm vir}$, and results in higher (lower) cool gas densities. The temperature of the cool gas is also slightly decreased (increased), enhancing the density change compared to nominal. On the other hand, for a fixed $\alpha_{\rm cool}$ profile, lower (higher) nonthermal support in the hot gas gives higher (lower) η , opposing the effect of higher (lower) ambient gas pressures, and producing cool gas densities similar to those in the nominal model.

6.2. Radiation

In this work we assume that the heating and photoionization of the cool CGM are dominated by the MGRF, and adopt the HM12 field. In this section we first discuss our choice of the MGRF, then examine a possible contribution from galactic radiation, and address our assumption of optically thin gas. In our discussion we address the spatially averaged ionizing photon flux (E > 13.6 eV), given by $\Phi = \int J_{\nu} d\nu$ and depending on the radiation field intensity and spectral shape.

6.2.1. Metagalactic Radiation Field

For this work, we focus on the ionizing flux at z < 0.5, dominated by photons at 13.6 < E/eV < 100. In this redshift and energy range, the MGRF is not well constrained empirically, and existing works have different predictions for the field spectral shape and intensity. For example, the fields

calculated by Faucher-Giguère et al. (2009) and (Khaire & Srianand 2019, hereafter KS19) predict Φ values that are higher than HM12 by a factor of ≈ 1.5 (see their Figure 7 for a comparison). In this work we adopt the HM12 field for consistency with FSM20 and verify that using the Khaire & Srianand (2019) field changes the resulting ions fractions by < 50%.

How will a higher Φ affect our inferred model parameters? For a given hot gas pressure profile, reproducing a measured column density ratio with higher ionizing flux would require increasing the (mean) gas volume density by a similar factor (see also P17 for discussion). In our model, this can be achieved by reducing the nonthermal support, η , by the same amount (see Equation (2)). Producing the same total ion columns with higher gas densities will require lowering the cool gas volume filling fraction, $f_{V,cool}$, and the total cool gas mass will be only weakly affected (see Equation (10)).

In this work we also adopt a single ionizing flux, $\Phi=2\times10^4$ photons s⁻¹, corresponding to z=0.2, the median galaxy redshift in our sample. Models show that at low z, the MGRF flux is a strong function of the redshift, following the decline in the cosmic SFR and SMBH activity since $z\sim2$. For the HM12 field at z<0.5, the flux evolution can be approximated by $\Phi\approx\Phi_0\times(z+1)^4$, resulting an increase of ≈3 from z=0.1 to 0.4, the full redshift range in our sample. This variation in ionizing flux may be one of the factors contributing to the scatter between the observed columns, and will be addressed in modeling of the individual lines of sight.

6.2.2. Local/Galactic Radiation

We now discuss a possible contribution of galactic radiation, from an AGN, stars, stellar remnants, or outflows, to the ionization of the CGM.

Radiation from local sources is expected to fall off rapidly with the distance from the galaxy, as r^{-2} . This suggests that at small enough distances from the galaxy, galactic radiation will eventually become strong enough to significantly affect the gas ionization state (see Sternberg et al. 2002). Where does this happen? McQuinn & Werk (2018) estimated that local radiation sources (excluding AGN radiation) cannot be dominant beyond $r \sim 100$ kpc from the galaxy. Upton Sanderbeck et al. (2018) added emission from quasars to the background field, and find that at $z \sim 0.2$ the "proximity radius," at which galactic and extragalactic background sources contribute equally to the local radiation field, is $\sim 10-30 \text{ kpc} \times (\text{SFR/M}_{\odot} \text{ yr}^{-1})^{1/2}$. Holguin (2022) used hydrodynamic simulations and ionization modeling to show that stellar radiation has a negligible effect on the cool CGM at $r \gtrsim 30 \,\mathrm{kpc}$ ($\approx 0.1 \,R_{\mathrm{vir}}$) in MW-mass halos at low redshift. Radiation from an accreting SMBH can be highly nonisotropic and significant enough to affect gas at large distances from the galaxy. The COS-Halos galaxies do not harbor an AGN, but Oppenheimer et al. (2018b) found that radiation can have a lingering effect on the OVI, even after the AGN has switched off. Estimating the time-dependent effect of the AGN radiation on gas ionization is beyond the scope of this work.

Sarkar et al. (2022) performed simulations of winds driven by supernovae, including radiative transfer and nonequilibrium ionization effects. They compare the emission from the winds to the intensity of the MGRF, and find that close to the starforming regions, at d < 1 kpc, wind radiation can be orders of magnitude stronger than the background flux (see their Figure 3). However, at $r \sim 10$ kpc, the radiation intensity is

close to the background, and extrapolating to $r \sim 30 \,\mathrm{kpc}$, we expect the two components to be similar. Their simulations are run with SFR = $10 \, M_\odot \,\mathrm{yr}^{-1}$, and they compare to the $z=0 \,\mathrm{HM12}$ MGRF. Scaling these to the median SFR of the COSHalos sample, SFR = $4.3 \, M_\odot \,\mathrm{yr}^{-1}$, and the z=0.2 background flux should further lower the ratio of wind to background radiation by a factor of ~ 5 , and we estimate that radiation from winds should be subdominant at $r \gtrsim 14 \,\mathrm{kpc}$, or $\approx 0.05 \,R_\mathrm{vir}$, and possibly even closer to the galaxy.

We summarize that galactic radiation should not be dominant beyond $r \approx 0.1~R_{\rm vir}$, and our approximation that the ionization is dominated by the MGRF at large radii is reasonable. This radius may be larger for individual galaxies, with higher present or recent SFR, or past SMBH activity, and these may contribute to the scatter in the data at small impact parameters.

6.2.3. Optically Thin Gas

In this work, we assume the cool gas is optically thin. We calculate the ion fractions as functions of gas density and temperature in the presence of the MGRF for a wide range of gas properties using Cloudy (Ferland et al. 2017). Then, given the cool gas density and temperature spatial profiles in the model, set by pressure equilibrium with the warm/hot phase, we use these ion fractions to construct the ion density profiles as functions of radius. This calculation is fast and flexible, allowing us to construct different profiles and distributions using precomputed Cloudy data. However, since the ion fractions are calculated locally for small gas parcels in the presence of the unattenuated MGRF, this does not account for gas self-shielding from radiation at high column densities. We now discuss the validity of this approach.

Self-shielding by hydrogen becomes important at $N_{\rm H\ I} \gtrsim 1-3 \times 10^{17} \, {\rm cm}^{-3}$. In our data set, $\sim \! 3/4$ the systems are below this threshold, and almost all of the systems with higher H I columns occur at small impact parameters, at $h/R_{\rm vir} \lesssim 0.25$ (see Figure 3). Even for these lines of sight, most of the CGM volume is exposed to the MGRF through a lower column density of neutral hydrogen, and only gas close to the galaxy may be self-shielded. In this innermost region, our model is most uncertain for other reasons, such as deviation from spherical symmetry and hydrostatic equilibrium, effects of galactic outflows, and galactic radiation (Section 6.2.2).

We can estimate qualitatively how including the effects of gas self-shielding will affect our results. For given model parameters (η and $f_{V,cool}$), an attenuated radiation flux will lead to a lower ionization parameter, and higher fractions of the lower ions, such as HI, CII, SiII, and MgII, and lower fractions of higher ions (CIII, CIV, Si III, Si IV). As noted earlier, in the presence of MGRF (no galactic radiation), this effect may be nonnegligible only in the inner region of the halo, resulting in slightly steeper (flatter) column density profiles as functions of the impact parameter for the low (higher) ions. We can use Figure 9 to estimate how such ratio change will affect our parameter inference. For example, a lower MGRF flux will lead to a higher CII/CIII column density ratio, and to reproduce a measured ratio at a given impact parameter, our models will require a higher η (left panel), compared to the optically thin gas case. Similarly, shielding will produce higher HI column densities, leading to lower volume filling fraction, or cool gas mass, implied by a given measured column (right panel).

To summarize, we argue that our assumption of optically thin gas is valid for a large fraction of our data set and most of the volume of the CGM. It may break down at small distances from the central galaxies, where our model has the largest uncertainties for additional reasons. Accounting for self-shielding may lower the cool gas mass and increase the nonthermal support inferred values, compared to the calculation presented in this work. However, we estimate that these effects will be small, and limited to systems with high H I columns measured at small impact parameters. We plan to include self-shielding in our model in future work.

7. Discussion

The model presented in this work allows us, when applied to observations, to constrain the mass, metallicity, and spatial distribution of the cool CGM (Sections 4 and 5.3). While the model itself is intentionally agnostic to the source of the cool gas or its formation mechanism, the results of our analysis may favor, or be more consistent, with some mechanisms over others. We now discuss constraints on the cloud sizes, the depletion time of cool CGM, and possible channels for its buildup or replenishment.

7.1. Cool Gas: Cloud Sizes

Our model constrains the volume filling factor of the cool CGM, and does not address the sizes of individual clouds. We now show that combining the model volume filling factor with the sky covering fraction estimated from observations allows us to place some constraints on cloud sizes.

The volume number density of cool clouds at some distance from the galaxy can be written as by $n_{\rm cl} = (dV_{\rm cool}/V_{\rm cl})/dV = f_{\rm V,cool}/V_{\rm cl}$, where $V_{\rm cl}$ is the volume of a single cloud, and we used the definition of $f_{\rm V,cool}$ (Equation (3)). The number of clouds along a line of sight through the CGM is then

$$N_{\rm cl}(h) = \int_{S} A_{\rm cl} n_{\rm cl} ds = \int_{S} \frac{A_{\rm cl}}{V_{\rm cl}} f_{\rm V,cool} ds = \frac{3}{4} \int_{r_{\rm l}}^{r_{\rm 2}} \frac{f_{\rm V,cool}}{R_{\rm cl}} ds,$$
(12)

where $A_{\rm cl}$ is the cloud cross section, and for the last equality, we assumed spherical clouds.

For simplicity, we assume a cloud size that is constant with radius, giving $N_{\rm cl} \propto \sqrt{1-h^2/r_2^2}/R_{\rm cl}$. In Figure 11 we plot $N_{\rm cl}$ as a function of the impact parameter, for cloud sizes of $R_{\rm cl}=0.2,\ 0.6,\$ and 2 kpc (dashed, solid, and dotted black curves, respectively), for our nominal model, with $f_{\rm V,cool}\approx 1\%$. For $R_{\rm cl}=0.6$ kpc, the number of clouds decreases weakly from $N_{\rm cl}\approx 5$ at h=0.1 $R_{\rm vir}$ to 3 at h=0.4 $R_{\rm vir}$ and steeply after that. For $R_{\rm cl}=0.6$ kpc, we also plot $N_{\rm cl}$ for the extended model (solid blue curve).

For a small number of clouds, we expect the detection rate to vary significantly between lines of sight, and for $N_{\rm cl} < 1$ (shown by the solid magenta line) we also expect the detection rate to be low. However, W14 reported a detection rate, or sky covering fraction, close to unity for all impact parameters. Furthermore, they estimated an average of $\approx 2-3$ spectral components per line of sight in the COS-Halos data. This range, shown by the magenta band, can be taken as a lower limit on the number of clouds per line of sight, due to limited spectral resolution of COS and possible clustering of individual gas clouds in the CGM. For $R_{\rm cl} = const.$, we can rewrite

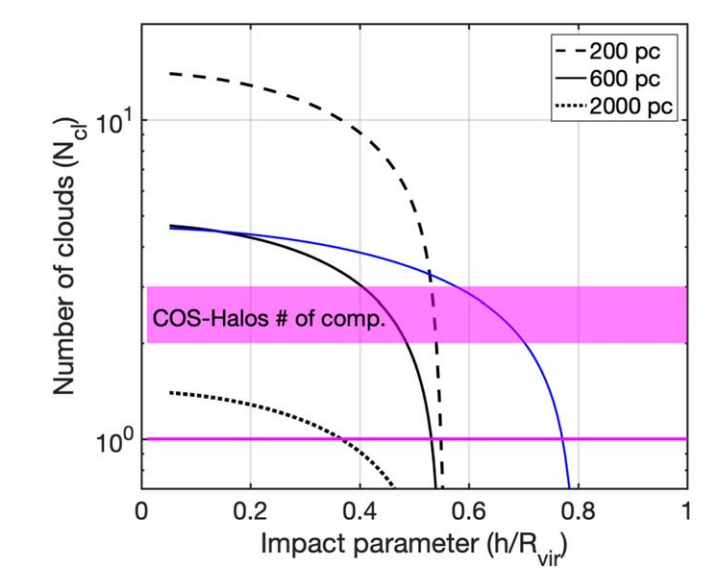


Figure 11. Number of clouds along a line of sight as a function of the impact parameter, for different clouds sizes. The black curves show the distribution for the nominal model, and the solid blue—for the extended model (see Section 4). The horizontal magenta lines show $N_{\rm cl} = 1$ (solid) as an approximate threshold for high detection rate, and $N_{\rm cl} \approx 2.4$ (shaded band) is the average number of spectral components per line of sight in COS-Halos (W14).

Equation (12) as a constraint on cloud size

$$R_{\rm cl}(h) = \frac{3r_2 f_{\rm V,cool}}{2N_{\rm cl}} \sqrt{1 - h^2/r_2^2}$$

$$\lesssim 0.40 \left(\frac{f_{\rm V,cool}}{0.01}\right) \left(\frac{N_{\rm cl}}{3}\right)^{-1} \left(\frac{r_2}{150 \text{ kpc}}\right) \text{kpc}, \quad (13)$$

estimated at $h=0.85r_2$, and a factor of ≈ 2 larger at $0.15\,R_{\rm vir}$ (for $R_{\rm vir}=260\,{\rm kpc}$). We conclude that for our nominal model, $R_{\rm cl}\gtrsim 1.5\,{\rm kpc}$ predicts less than one cloud per line of sight and is inconsistent with the observed high detection rates, and for $N_{\rm cl}\gtrsim 3$, $R_{\rm cl}\lesssim 0.5\,{\rm kpc}$. The mass of an individual cloud at a given radius then scales as the local gas density, and can be written as

$$M_{\rm cl}(r) = 1.67 \times 10^4 \left(\frac{r}{100 \,\mathrm{kpc}}\right)^{-a_{\rm n,c}} \left(\frac{\eta}{3}\right)^{-1} \left(\frac{R_{\rm cl}}{0.5 \,\mathrm{kpc}}\right)^3 M_{\odot},$$
(14)

where $a_{\rm n,c} \approx 1.67$ for our nominal model (see Table 1).

We can also apply our estimate for $R_{\rm cl}$ to the IT gas scenario examined in Section 5.2. The cloud size is linear with the gas volume fraction, and for $f_{\rm V,IT}=40\%$, we get $R_{\rm cl,IT}\lesssim 16$ kpc. We note that if the cool and IT phases coexist as cool clouds surrounded by warm gas envelopes, as suggested by the mixing layers scenario, these structures are dominated by intermediate-temperature gas in volume, with very small cool gas cores. This is different from the picture seen in numerical simulations, with relatively thin warm gas interfaces around cool gas clouds.

For a given total mass in cool gas, variation in η will affect the number of clouds through the volume filling factor. As discussed Section 4, lower η corresponds to higher gas densities and requires lower $f_{V,cool}$ (see left panel of Figure 2, and Equation (9)), resulting in a stronger constraint on cloud size. For the low (high) η model presented in this work, the

number of clouds of a given size will be a factor of \approx 3 lower (higher).

The upper limit we estimate for $R_{\rm cl}$ can be compared to previous observational estimates. W14 estimated the cloud sizes as the ratio of the total gas column to the local density, l=N/n, and found a median of 10^{+35}_{-10} kpc, with a wide range, 0.1–2000 kpc. Since this estimate assumes a single cloud for each line of sight, it provides an upper limit for the cloud size, and the median is consistent with our result. They then infer the gas volume filling fraction using the cloud size (assuming spherical geometry) and the sky covering fraction, adopting the method described by Stocke et al. (2013), and infer $f_{\rm V,cool} \approx 11^{+05}_{-9}$ %. While these are higher than the values we infer, they are consistent within the estimated errors with our range, of $\approx 0.5\%$ –10%. For comparison, Stocke et al. (2013) examined a different data set and estimated a median cloud size of 1 kpc with a ± 1 dex range.

Zahedy et al. (2021) used absorption observations of lensed quasars to probe coherence of cloud properties across small spatial scales. They found that at separations below $\sim\!0.15$ kpc, there is little variation in the column densities and velocities of absorbers (see also Rubin et al. 2015, 2018; Rudie et al. 2019, and Augustin et al. 2021 for similar studies at higher redshifts). Our constraint is consistent with this result, and if cloud sizes are indeed close to 0.15 kpc, our calculation suggests $\approx\!10$ individual cool gas clouds along a line of sight in the nominal model.

McCourt et al. (2018) argued that gas undergoing thermal instability and cooling fragments (or "shatters") into smaller and smaller clouds, and the cloud size at the end of this process is given by the cooling length

$$L_{cs} = c_s t_{cool} = \left(\frac{k_B T}{\bar{m}}\right)^{1/2} \frac{n k_B T}{n_e n_H \Lambda}$$

$$\approx 90 \left(\frac{n}{10^{-3} \text{ cm}^{-3}}\right)^{-1} \left(\frac{T}{10^4 \text{ K}}\right)^{3/2} \text{ pc}, \tag{15}$$

where in the last approximation we used $\Lambda = 10^{-23}\,\mathrm{erg}\,\mathrm{s}^{-1}\,\mathrm{cm}^3$, the net-cooling efficiency of gas at $T \sim 10^4$ K. Equation (15) shows that for the densities of the cool phase in our models $(n \sim 10^{-4} - 10^{-2}\,\mathrm{cm}^{-3};$ see middle panel of Figure 1), clouds in the CGM have sizes of $\sim 10-1000$ pc, significantly larger than the subparsec-scale clouds estimated by this equation for ISM densities. Our limit in Equation (13), using the observed gas covering fraction, agrees with this size estimate at $h \lesssim 0.6\,R_{\rm vir}$.

The analysis presented here is highly simplified. The sizes of clouds do not have to be constant with distance from the galaxy if the properties of the ambient medium and the cool gas vary significantly. Cloud sizes may also be set or affected by additional physical processes other than cooling-turbulence and instabilities, for example, can disrupt clouds and break them to smaller sizes (Armillotta et al. 2017), while magnetic fields may protect the clouds from fragmentation (Sparre et al. 2019). Given these various mechanisms, the assumption of spherical geometry is also a simplification, and clouds that are infalling or magnetized may be stretched into filaments (see Tan & Fielding 2023, for example). Finally, clouds may have a distribution of sizes, possibly related to their different origins (see Section 7.2), and they may cluster and form complexes and larger structures, such as those observed in the MW (Putman et al. 2012) and suggested by higher-resolution spectra

(Tripp 2022). Given this potential complexity, we find the agreement between our results and other (observational and theoretical) works encouraging, and leave a more detailed study of cloud sizes, shapes, and kinematics for future study.

7.2. The Cool CGM Reservoir: Depletion and Formation

The dense cool gas clouds are not supported by the (hydrostatic) pressure gradient of the ambient gas, and may fall toward the galaxy. For a cloud starting at rest at a distance r from the halo center, the freefall time is given by

$$t_{\text{infall}}(r) \approx \left(\frac{\pi^2 r^3}{8GM(< r)}\right)^{1/2} \approx 2.3 \times 10^9 \left(\frac{r}{R_{\text{vir}}}\right)^{1.13} \text{ yr, } (16)$$

where we used the approximation for the Klypin et al. (2002) profile, and $R_{\rm vir} = 260$ kpc.¹⁶ This is similar to the result obtained by Shull & Moss (2020) for a pure Navarro–Frenk– White halo, with $t_{\rm infall} \sim 190$ Myr at r = 50 kpc. This estimate is a lower limit on the infall time for clouds starting at rest, since it does not include the effect of ram pressure from the hot medium, which will slow the clouds down (Afruni et al. 2021). Furthermore, clouds may be disrupted by hydrodynamical instabilities (see Joung et al. 2012b, for example), or grow through cooling-driven accretion from the hot phase and slow down (Tan et al. 2023). Thus, the accretion process of cool gas from the CGM onto the galaxy is highly uncertain. For our analysis here, we can use Equation (16) to estimate the mean accretion rate of cool gas, given by $\dot{M}_{\rm cool} \sim M_{\rm cool}/t_{\rm infall}$. For the nominal model presented in Section 4, with $M_{\text{cool}} = 3 \times 10^9 M_{\odot}$ and $r \approx 0.5$ $R_{\rm vir}$, this gives $\dot{M}_{\rm cool} \sim 3 \, M_{\odot} \, {\rm yr}^{-1}$, and $\sim 1-10 \, M_{\odot} \, {\rm yr}^{-1}$ for the models in the mass set. The COS-Halos star-forming galaxies have star formation rates in the range of $0.6-19 M_{\odot} \text{ yr}^{-1}$, with a median of $4.3 M_{\odot} \text{ yr}^{-1}$ (Werk et al. 2013, and Table A1 here), and we find this agreement reasonable. We note that our nominal result is also similar to the MW SFR, with $\approx 1.6 - 2.0 M_{\odot} \text{ yr}^{-1}$ (Chomiuk & Povich 2011; Licquia & Newman 2015). Fox et al. (2019) estimated an inflow rate of $\sim 0.5 \, M_{\odot} \, {\rm yr}^{-1}$ from observations of HVCs in the MW, and commented that the actual mass inflow rate may be higher due to gas at lower velocities.

The high detection rate of cool CGM in the COS-Halos survey suggests that the reservoir of cool gas in the CGM is long-lived rather than a transient phenomenon. This can happen if accretion occurs on timescales significantly longer than the dynamical time (as noted earlier), or the cool gas is continuously replenished, resulting in a low net depletion rate. We now discuss the latter scenario.

Cool gas can form or be added to the CGM by different mechanisms, including accretion from the IGM (Kereš et al. 2005; Dekel et al. 2009; Wright et al. 2021), stripping from satellite galaxies (Tonnesen & Bryan 2009; Putman et al. 2021), condensation from the warm/hot ambient medium (Joung et al. 2012a; Sharma et al. 2012; Voit 2019), and outflows from the galaxy (Li & Bryan 2020; Fielding & Bryan 2022). We now address the possible contribution from each of these channels.

Correa et al. (2015) modeled cosmological accretion and found that for a $10^{12}\,M_\odot$ halo at $z\sim0.2$, baryons are added to halos at a rate of $\dot{M}\sim8.2\,M_\odot$ yr⁻¹, linear with $M_{\rm vir}$ (see their Equation (23)). Fakhouri et al. (2010) reported similar results, with slightly higher accretion rates (up to $\approx40\%$). For massive halos at low z, we expect the infalling gas to shock around the virial radius and contribute mainly to the warm/hot phase of the CGM. However, some fraction may contribute directly to the cool gas, either by accretion through streams penetrating the virial shock (Mandelker et al. 2017), or infall of massive clouds that are not completely disrupted (Afruni et al. 2022).

Satellite galaxies can contribute some cool gas to the CGM. For example, the gas stripped or expelled from the LMC is responsible for the Magellanic Stream and (possibly) the Leading Arm. Putman et al. (2021) showed that the small dwarf galaxies inside the virial radius of the MW and M31 are all gas poor, while a few dwarf galaxies detected at larger distances have retained their gaseous components (Ryan-Weber et al. 2008; Giovanelli et al. 2013). Presumably, at least some of the gas content of the accreted satellites was added to the MW cool CGM reservoir, and we expect the same to happen in other galaxies (see also Nateghi et al. 2021).

Cooling from the warm/hot phase can also contribute to the cool phase through condensation and cloud formation, although the transformation between gas phases in the CGM is highly uncertain. Addressing the conditions for condensation and precipitation, Sharma et al. (2012) found that warm/hot gas with a low ratio of cooling to dynamical time, $t_{\rm cool}/t_{\rm dyn}$ is more susceptible to condensation. This was adopted by Voit (2019) as the main parameter regulating gas accretion onto the galaxy in the precipitation model (however, see Esmerian et al. 2021). In the FSM20 fiducial model, $t_{\rm cool}/t_{\rm dyn}$ decreases with distance from the galaxy, and $t_{\rm cool}/t_{\rm dyn}(r > 50~{\rm kpc}) \sim 4$, below the threshold of 10 estimated in McCourt et al. (2012) and adopted in the precipitation model. This suggests formation of cool gas occurs at large distances from the galaxy, consistent with the extended cool gas distribution in the COS-Halos data, and in our model. After formation, the cool gas may migrate inward (see A. Cruz et al. 2023, in preparation). This is qualitatively different from the picture in Maller & Bullock (2004), for example, where the cool gas forms at small radii first, where the absolute dynamical and cooling times are shorter (see also Marinacci et al. 2010 and Fraternali 2017 for fountain- and accretion-induced condensation close to the galactic disk).

For example, in the FSM20 fiducial model, the global, mean mass cooling rate of the warm/hot CGM is $13.3\,M_\odot\,{\rm yr}^{-1}$. Faerman et al. (2022) calculated the cooling rate of the warm/hot CGM as a function of the CGM mass for a sample of galaxies generated by the Santa-Cruz semianalytic model (Somerville & Primack 1999; Somerville et al. 2008, 2015). They get a similar result, with $\dot{M}_{\rm w/h}\approx 9.4\times 10^{0.21\sigma}\times (M_{\rm hot}/5\times 10^{10}\,M_\odot)^{1.64}\,M_\odot\,{\rm yr}^{-1}$, where σ accounts for the distribution in metallicity at a given CGM mass. While the FSM20 model assumes that the warm/hot gas is in equilibrium, and the cooling rate is balanced by heating from galactic feedback, the balance does not have to be perfect. Some fraction of the net mass cooling rate of the warm/hot CGM may accrete directly onto the galaxy (Joung et al. 2012b), and the rest can replenish the cool CGM reservoir.

Finally, galactic outflows are commonly observed in starforming galaxies in the low-redshift universe (Rupke et al. 2005;

 $[\]overline{^{16}}$ FSM20 adopted the dynamical time used by Voit (2019), $t_{\rm dyn} = \sqrt{2r^3/GM(< r)}$, a factor of ≈ 1.3 longer.

Martin et al. 2012; Bolatto et al. 2013; Chisholm et al. 2017; Werk et al. 2019; Rubin et al. 2022) and can add cool gas to the CGM (see Fraternali 2017; Veilleux et al. 2020 for reviews). Mass outflow rates are challenging to estimate observationally due to uncertainties in gas ionization fractions, metallicities, velocity distributions, and geometry. Chisholm et al. (2017) used UV observations to study outflows in a sample of nearby galaxies with $10^7 < M_*/M_\odot < 10^{11}$. For MW-mass galaxies, with $M_* \sim 5 \times 10^{10} \, M_\odot$, they infer a mass loading factor of $\dot{M}/\rm{SFR} \approx 0.3$ (see their Figure 1). For SFR $\approx 4.3 \, M_\odot \, \rm{yr}^{-1}$, the median of the COS-Halos sample, this corresponds to an outflow rate of $\approx 1.3 \, M_\odot \, \rm{yr}^{-1}$, and suggests galactic winds can offset a significant fraction of the cool gas accretion rate. In the MW, Fox et al. (2019) used metal absorption in HVCs to estimate $\dot{M} \approx 0.16 (Z'/0.5) \, M_\odot \, \rm{yr}^{-1}$, providing a lower limit to the total outflow rate.

Outflow rates are easier to calculate in hydrodynamical simulations, although they may depend on the feedback implementation. For $10^{12}\,M_\odot$ halos at z<0.5, recent numerical studies of galaxy disks (Kim et al. 2020; Barbani et al. 2023) and cosmological zoomed-in simulations (Christensen et al. 2016; Tollet et al. 2019; Pandya et al. 2021) find $\dot{M}/\rm{SFR}\sim0.1$ –0.5, similar to the observational estimates. Mitchell et al. (2020) found values higher by a factor of 2–3 in EAGLE, suggesting outflows may be dominant in replenishing the cool CGM.

However, in nonstarburst galaxies, the spatial extent of winds may be limited, and this channel is probably more significant close to the galaxy, at $r \lesssim 10-30$ kpc. As shown in Section 4.2, the measured columns are consistent with an extended distribution of cool gas, with $r_{\rm out} \gtrsim 0.6 R_{\rm vir} \approx 150$ kpc, and possibly all the way out to the virial radius. This large spatial extent suggests that the buildup of the cool CGM reservoir took place at earlier times, when SFR were significantly higher, or through a different channel. Furthermore, the metallicity of $Z' \sim 0.3$ is lower than expected from enriched galactic outflows and than the metallicity of the warm/hot gas in the fiducial FSM20. This may suggest that either (i) the cool phase is less dominated by outflows, or (ii) mixing of enriched outflowing gas with metal-poor inflows is less efficient for the cool phase than in the more diffuse warm/ hot medium.

Related to this discussion, a series of recent studies explored different scenarios for the origin of the cool CGM in lowredshift galaxies (Afruni et al. 2019, 2021, 2022). For example, Afruni et al. (2021) modeled the kinematics of the cool gas in the COS-Halos galaxies with an outflow scenario. They found that the COS-Halos cool gas cannot be a result of supernovae outflows, since the energy required for that would be more than that available in supernovae events. Afruni et al. (2019) and Afruni et al. (2022) performed similar modeling of the cool CGM of quiescent galaxies (COS-LRG; Chen et al. 2018) and of M31 (AMIGA; Lehner et al. 2020) and obtain similar results, concluding that most of the cool gas comes from IGM accretion. In these works, most of the cool clouds are at large radii from the galaxies, resulting in a flat column density distribution with impact parameter (see Figure 5 in Afruni et al. 2022). We find that gas has to be distributed across a range of radii, from close to the galaxy and possibly out to R_{vir} , to

reproduce the binned steep profiles of H I and the low metal ions (see Figures 3–6).

To summarize, we have shown that the reservoir of cool CGM can be replenished in several ways, either through accretion from the IGM (smooth or lower-mass halos), condensation from the warm/hot phase, or outflows from the galaxy. The estimated rates suggest that even if the cool CGM accretes onto the galaxy at a rate equal to the SFR, its net depletion rate can be close to zero, leading to a mean constant mass of cool gas in the CGM, and approximate equilibrium on long, possibly cosmological timescales. It is interesting to note that in the COS-Halos sample, lines of sight probing the CGM of quiescent galaxies show similar ionization states and column densities. Other observational studies of cool gas around quiescent galaxies at z < 1found similar results (Zahedy et al. 2019; Chen et al. 2020; Ou et al. 2022). This work does not aim to answer the question of what causes galaxies to stop forming stars and what part the (cool) CGM plays in it (see Tchernyshyov et al. 2023 for OVI-bearing gas). Our model can be applied to observations of quiescent galaxies in a future study.

8. Summary

In this work we presented a detailed model for the cool, photoionized phase of the CGM that includes density variation with radius, allows for nonthermal pressure, and addresses the gas thermal and ionization state. This work expands the modeling framework presented in FSM20 for the warm/hot CGM, which reproduces the O VI absorption measurements in the extended CGM of MW-mass, SF galaxies at low redshifts, reported by the COS-Halos survey (Tumlinson et al. 2011). In this study, we aimed to reproduce the average cool CGM of these galaxies, traced by absorption of neutral hydrogen and low to intermediate metal ions, also reported by COS-Halos (Werk et al. 2012; Prochaska et al. 2017). Applying our model to the column density measurements allowed us to constrain the cool gas mass, deviation from thermal pressure equilibrium, spatial distribution, and morphology.

Our key points and results are as follows:

- 1. We present a model setup for cool gas in heating/cooling and photoionization equilibrium with the MGRF (Section 3). We assume that the cool gas in the CGM is in total pressure equilibrium with the warm/hot, volume filling phase, allowing it to be long-lived, consistent with the high detection rate measured in the COS-Halos survey. Our model aims to be flexible yet simple, with free parameters for (i) nonthermal support in the cool gas, allowing cool gas densities lower than expected from thermal pressure equilibrium, (ii) spatial extent, and (iii) volume filling fraction, setting the cool gas mass (Figures 1–2).
- 2. We show that a nominal model with $M_{\rm cool} = 3 \times 10^9 \, M_{\odot}$ and $\eta = P_{\rm hot,th}/P_{\rm cool,th} = 3$ is consistent with the mean column density profiles of neutral hydrogen (Figure 3) and low/intermediate metal ions (C II, C III, Si II, Si III, and Mg II; Figures 4–6). This suggests that extreme scenarios, with high cool gas masses or nonthermal pressure support, are not necessary to explain the cool CGM of an average galaxy. In this nominal model, the cool gas occupies $\sim 1\%$ of the total CGM volume and extends to $\sim 0.5 R_{\rm vir}$ (although more extended distributions cannot be ruled out).

¹⁷ We do not discuss winds driven by accretion onto SMBHs since the COSHalos galaxies do not host AGNs. While the effects of past AGN-driven outflows may be important, addressing these is beyond the scope of this work.

- 3. Models with variation of ± 0.5 dex in the gas mass and nonthermal support allow us to reproduce the typical scatter in the measured column densities and $\sim \! 2/3$ of the individual measurements (Section 4). Variation in the gas spatial extent can also reproduce the observed low H I column densities. The model outputs are presented and compared to observations in Figures 3–6. These models, varying a single parameter each time, underpredict the measured column densities of C IV and Si IV.
- 4. We address two scenarios that reproduce the high observed H I, C IV, and Si IV column densities (Section 5.1 and Figure 7). First, we show that combinations of high mass $(10^{10}\,M_\odot)$ and low or high nonthermal support $(1<\eta<5)$ reproduce high H I or C IV and Si IV, respectively. Second, we show that the high metal ions can, in principle, form in intermediate-temperature gas, cooling from the hot phase or in residing in mixing layers around the cool clouds. However, this scenario requires a high volume filling fraction $(\sim 1/2)$ and high mass $(\sim 1.5 \times 10^{10}\,M_\odot)$, in tension with the results of recent numerical studies.
- 5. We present a brief exploration of the model parameter space (Section 5.2), and show that for a volume filling fraction and metallicity that are constant with radius, columns of H I and two metal ions allow us to estimate the gas metallicity, mean volume density, and total mass for a given object/sight line (Figures 9–10).
- 6. We examine how our results are affected by the assumed distribution of the warm/hot ambient medium, the MGRF ionizing flux, and gas self-shielding (Section 6). We also show that for the typical SF galaxy, radiation from the central galaxy or galactic outflows is probably subdominant beyond ~15–30 kpc, or 0.05–0.10 $R_{\rm vir}$, and that our assumption of optically thin gas is valid for most of the CGM volume and lines of sight in our data set.
- 7. We show that the cool gas volume filling fraction combined with the measured sky covering fraction, provides an upper limit on the cloud sizes (Section 7.1). For our nominal model, $R_{\rm cl} \lesssim 0.5$ kpc is consistent with a covering fraction of ~ 1 and ≈ 3 absorption components (Figure 11). This limit is consistent with observational estimates and similar to the cloud sizes produced by thermal shattering for the gas densities in our models.
- 8. We estimate a mean accretion rate of $\sim 3\,M_\odot\,{\rm yr}^{-1}$ for our nominal model, similar to the median star formation rate in the COS-Halos galaxies. We then discuss possible channels for cool gas formation in the CGM (Section 7.2), including accretion from the IGM, condensation, and galactic outflows. We show that the cool gas in the CGM can be in a state of approximate equilibrium, consistent with its high detection rate in observations.

There is more work to be done, and this study is just the first step. Modeling of individual sight lines, rather than the mean columns, will allow us to further test the model, and may provide insights into the relation between galaxy and CGM properties. In this work we assumed that the gas metallicity, volume filling fraction, and the nonthermal support are constant functions of radius. The distributions of these properties in reality are probably more complex, and different scenarios can be tested with our model framework in the future. Finally, applying this model to data probing larger distances, and to the CGM of galaxies residing in a wider range of halo masses and SF rates may allow us to test different mechanisms for the formation of cool gas in the CGM, its interaction with the warm/hot gas, and the role the multiphase CGM plays in galaxy formation and evolution.

The manuscript is accompanied by 11 data files in machine readable format. The files list the model outputs as functions of the radius and impact parameter, for the warm/hot, cool, and intermediate gas distributions presented in this paper, to allow for comparison to observations and other models. The provided data were used to produce Figures 1–7. Additional data can be provided upon request to the authors.

Acknowledgments

We thank Greg Bryan, Akaxia Cruz, Thomas Do, Drummond Fielding, Cassie Lockhhaas, Chris McKee, Matt McQuinn, Stella Ocker, Kartick Sarkar, Rachel Somerville, Amiel Sternberg, Kirill Tchernyshyov, and Fakhry Zahedy for helpful discussions during the course of this work. We thank Matt McQuinn for their questions, suggestions, and comments on the manuscript. Y.F. thanks Chris McKee and Amiel Sternberg for collaboration on previous incarnations of this project and for discussions during this work. Y.F. thanks Liam Becker and Cyrus Taidi for the discussions held during the UW Pre-MAP project, and the CCA for hospitality during the TAU-CCA workshop. This research was supported by NASA award 19-ATP19-0023 and NSF award AST-2007012. J.K.W. gratefully acknowledges support from the Research Corporation for Science Advancement under grant ID No. 26842, and from the NSF-CAREER 2044303. This work also benefited from discussions held during the program "Fundamentals of Gaseous Halos" at the KITP (UCSB), supported by the National Science Foundation under grant No. NSF PHY-1748958.

Appendix A Summary of Observational Data

In Table A1 we list the properties of the galaxies in the sample addressed in this study (redshift, stellar mass, and star formation rate), the sight lines through the CGM (impact parameter, physical, and normalized to $R_{\rm vir}$), and the hydrogen and metal column densities reported for them. The galaxy properties are taken from Werk et al. (2012; their Table 4), and the absorption measurements are taken from Werk et al. (2013; their Table 4) and P17 (their Tables 2 and 3). All of the data are taken as is and provided for ease of comparison to the models presented in this work.

Faerman & Werk

Table A1
Observational Data Summary

SDSS Field	Galaxy ID	z	$\log(M^*/M_{\odot})$	SFR $(M_{\odot} \text{ yr}^{-1})$	h (kpc)	$h/R_{ m vir}$	НІ	Сп	C III	C IV	Si II	Si III	Si IV	Mg II
J0401-0540	67_24	0.2197	10.14	1.14 ± 0.15	83	0.35	$15.39^{+0.06}_{-0.05}$	<13.58	>14.00		<12.54	12.88 ± 0.06	<13.07	<12.26
J0910+1014	34_46	0.1427	10.61	14.42 ± 1.64	112	0.34	$17.71^{+0.23}_{-0.26}$	14.16 ± 0.06	•••	14.10 ± 0.09	12.96 ± 0.08	>13.28	•••	>13.29
J0914+2823	41_27	0.2443	9.81	2.83 ± 0.34	101	0.51	$15.40^{+0.05}_{-0.06}$	<13.64	•••	•••	<12.63	12.63 ± 0.11	<13.12	<11.87
J0943+0531	227_19	0.3530	9.59	0.47 ± 0.11	92	0.55	16.28 ± 0.04	14.42 ± 0.09	>14.30		<13.25	<12.97		<12.44
J0943+0531	106_34	0.2284	10.79	4.52 ± 0.58	121	0.34	$15.94^{+0.45}_{-0.41}$	<13.67		•••	<12.70	12.89 ± 0.10	<13.40	<12.20
J1009+0713	204_17	0.2278	9.85	4.58 ± 0.61	60	0.29	$17.26^{+0.13}_{-0.13}$	14.37 ± 0.05	•••	•••	<13.16	>13.26	<13.44	12.68 ± 0.03
J1016+4706	274_6	0.2520	10.21	0.53 ± 0.06	23	0.10	$17.05^{+0.05}_{-0.05}$	14.68 ± 0.03	>14.58		13.81 ± 0.05	>13.87		>13.55
J1016+4706	359_16	0.1661	10.48	1.37 ± 0.17	44	0.15	$17.74^{+0.50}_{-0.94}$	14.27 ± 0.07			13.68 ± 0.06	>13.74		>13.34
J1112+3539	236_14	0.2467	10.31	5.68 ± 0.80	53	0.21	$16.68^{+0.52}_{-0.48}$	<13.91			<12.93	12.09 ± 0.11	>13.38	12.38 ± 0.09
J1133+0327	164_21	0.1545	10.08	1.83 ± 0.22	55	0.27	>15.09	<13.77			<13.07	<12.91		<13.07
J1233-0031	168_7	0.3185	10.53	3.42 ± 0.54	32	0.12	$15.52^{+0.07}_{-0.10}$	<13.65	>14.18	•••	<13.33	13.01 ± 0.10	•••	<12.39
J1233+4758	94_38	0.2221	10.76	4.38 ± 0.52	132	0.38	$16.74^{+0.06}_{-0.06}$	>14.49	•••	•••	13.45 ± 0.05	>13.44	13.38 ± 0.07	>13.37
J1241+5721	208_27	0.2178	10.04	1.06 ± 0.17	93	0.41	$15.21^{+0.08}_{-0.12}$	<13.43	•••	•••	12.84 ± 0.10	12.72 ± 0.09	13.28 ± 0.11	<12.32
J1245+3356	236_36	0.1925	9.84	1.05 ± 0.17	112	0.54	$14.66^{+0.06}_{-0.06}$	<13.57	13.52 ± 0.07	•••	<13.19	<12.33	<12.84	<11.92
J1330+2813	289_28	0.1924	10.32	1.99 ± 0.23	87	0.33	$17.01^{+0.11}_{-0.13}$	14.37 ± 0.05	>14.08	•••	13.49 ± 0.04	13.19 ± 0.04	<13.29	>13.36
J1342-0053	157_10	0.2270	10.93	6.04 ± 0.74	35	0.09	$18.82^{+0.07}_{-0.15}$	>15.13	>14.65	•••	>14.49	>13.98	13.49 ± 0.11	>14.08
J1419+4207	132_30	0.1792	10.61	3.77 ± 1.06	88	0.28	$16.89^{+0.18}_{-0.20}$	14.06 ± 0.08	1 > 14.11		13.28 ± 0.07	>13.29	<13.53	>13.21
J1435+3604	68_12	0.2024	11.09	18.96 ± 2.28	39	0.08	$19.73^{+0.09}_{-0.14}$	>14.61	>14.31		>14.24	>13.46	<13.29	>13.74
J1435+3604	126_21	0.2623	10.37	5.56 ± 0.70	83	0.32	$15.17^{+0.11}_{-0.10}$				<12.77	12.84 ± 0.10	<13.46	<12.21
J1437+5045	317_38	0.2460	10.14	4.29 ± 0.50	143	0.73	14.53 ± 0.12				<13.04	<12.82	<13.38	<12.22
J1445+3428	232_33	0.2176	10.40	2.60 ± 0.31	113	0.39	15.07 ± 0.06	<13.62			<13.01	<12.63	<13.21	<12.55
J1550+4001	97_33	0.3218	10.90	7.41 ± 0.96	150	0.48	13.86 ± 0.09	<13.98	<12.96	•••	<12.96	<12.71	•••	<11.53
J1555+3628	88_11	0.1893	10.53	3.77 ± 1.06	34	0.11	$17.31^{+0.15}_{-0.14}$	14.49 ± 0.05	>14.30		13.41 ± 0.05	>13.53	13.88 ± 0.12	13.26 ± 0.0
J1619+3342	113_40	0.1414	10.11	1.33 ± 0.17	97	0.39	14.96 ± 0.03	14.30 ± 0.04		13.90 ± 0.03	<12.42		13.19 ± 0.08	<12.23

Appendix B Radial Distributions of Metal Ions

In Section 4 we presented the column density profiles for models with different parameter combinations, and compared them to observations. We now present and discuss the underlying radial profiles of the ion fraction and ion volume density for carbon. The neutral hydrogen fraction is approximately proportional to the gas density, and the silicon ions are similar in their behavior to the carbon ions. The radial fraction and density profiles for all of the ions discussed in the paper are available in the data files attached to this manuscript.

We focus on the models in the pressure set (#1), which vary in the value of η , the amount of nonthermal pressure in the cool gas, affecting the gas density and the ion fractions. The profiles for the models in the other sets can be calculated from the profiles of the nominal model, and we address this at the end of this section.

The top panels of Figure B1 show the ion fractions of C II (left panel), C III (middle), and C IV (right). In the nominal model (solid curve), the C II fraction decreases rapidly with distance from the halo center, as the gas density decreases and it becomes more ionized. The fraction of C IV shows an opposite trend, increasing strongly with r. The C III fraction decreases with radius up to $r \sim 0.5 R_{\rm vir}$ and decreases at larger

radii, and it is higher than 0.1 almost everywhere in the halo. The low- η model (dashed curves) has higher gas volume densities (see middle panel of Figure 1), leading to less ionized gas compared to the nominal model. As a result, the C II (C IV) fraction is higher (lower), by about an order of magnitude at $r \sim 0.6R_{\rm vir}$. The high- η model (dotted curves) has lower gas densities, resulting in lower (higher) C II (C IV). In all three models, the C II fraction peaks close to the halo center, where gas density is highest, with $f_{\rm C~II} \sim 1$. For C IV, the fraction is highest close to or at the outer boundary, and does not go above $f_{\rm C~iv} \sim 0.3$, the maximal C IV fraction in photoionized gas.

The bottom panels of Figure B1 shows the ion volume densities, given by the product of the ion fractions (shown in the top panels), solar carbon abundance, $A_C = 2.7 \times 10^{-4}$, model metallicity, Z' = 0.3 solar, and the hydrogen density profiles, plotted in the middle panel of Figure 1.

The C II densities decrease rapidly with radius due to a combination of the steep gas density and ion fraction radial profiles, resulting in steep volume density profiles and steep column density profiles as function of impact parameter (see top panels of Figure 4). The low- (high-) η model has higher (lower) densities and C II fractions, leading to C II densities higher (lower) by 0.5–1.0 dex than in the nominal model at all radii. The shape of the C III fraction profile leads to a weak variation in the volume density, of 0.5–1.0 dex, across the full

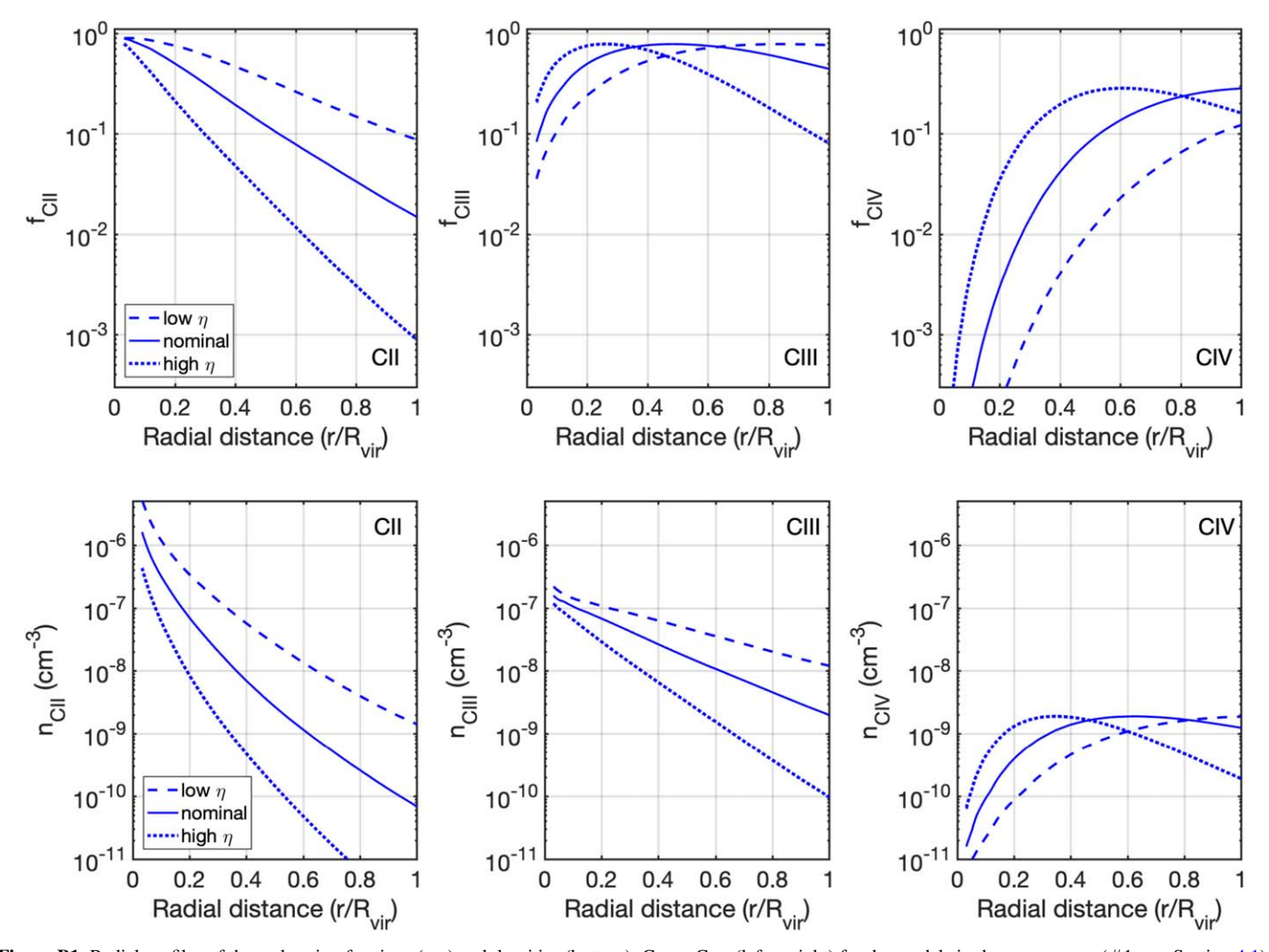


Figure B1. Radial profiles of the carbon ion fractions (top) and densities (bottom): C II to C IV (left to right) for the models in the pressure set (#1; see Section 4.1). The model outputs used in this figure are available in machine-readable format.

radial range. The difference between models is also smaller here, with a maximum of ~ 0.5 dex at $r \sim 0.5$ $R_{\rm vir}$. Finally, the C IV fraction increases more rapidly with radius than the gas density decreases, resulting in much smaller variation in the volume density. The opposite trends of the gas density and ion fraction lead to the C IV being lower (higher) in the low- (high-) η model compared to the nominal model. The steep profiles can be approximated by a thick shell distribution, and result in close to flat column density profiles for C IV (bottom panels of Figure 4).

Finally, the ion fractions and volume densities presented can be used to easily calculate the profiles for additional models, including those in model sets #2 and #3. First, the ion fractions are not affected by the gas radial extent, r_2 , or the gas volume filling fraction, $f_{V,cool}$, and their profiles are identical for models with the same density profile and different combinations of r_2 and $f_{V,cool}$. For the models in the radius and mass sets (#2 and #3), the ion fraction profiles are identical to those of the nominal model presented here. Second, the ion volume densities in our models are proportional to $f_{V,cool}$, and can be calculated by scaling the profiles of the nominal model by the ratio of the volume filling factors, given in Table 1.

Appendix C Gas Volume Fraction Variation with Radius

In this study we assumed that the cool gas volume filling fraction, $f_{V,cool}$, is constant as a function of distance from the galaxy between r_1 and r_2 , the inner and outer boundaries of the cool gas distribution, respectively (see Section 3). This was done to keep the model simple, and as shown in Section 4, it is enough to reproduce the average column density profiles. Furthermore, any choice for the behavior of $f_{V,cool}$ with radius implies an assumption about the origin or formation mechanism of the cool gas (see Section 7.2), which we tried to avoid in this work.

We now briefly examine the effect of a radial variation in $f_{\rm V,cool}$ on the observables. To do this, we construct models in which the volume filling fraction decreases as a power-law function, $f_{\rm V,cool}(r) \propto r^{-a_f}$ with $a_f > 0$, representing a scenario in which cool gas is more abundant in the central region of the halo, possibly as a result of galactic winds. Similar to the models presented in Section 4, we keep the total cool gas mass in these test models fixed at our nominal value, $M_{\rm cool} = 3 \times 10^9 \, M_{\odot}$ (see Table 1).

Figure C1 shows the column densities for CII, Si II, and Mg II for models with $a_f = 1$ and $a_f = 2$ (dashed and dotted curves, respectively) comparing them to the nominal model presented in Section 4, with $a_f = 0$ (solid curve) and to observations. As expected, larger values of a_f lead to steeper column density profiles. Since the total cool gas mass is fixed, models with $a_f > 0$ have higher columns at impact parameters $<0.2 R_{\rm vir}$, and lower columns at larger projected distances. At $h/R_{\rm vir} \approx 0.3$ –0.4, the difference in column densities between the nominal model and a model with $a_f = 2$ is $\Delta N \approx 0.3$ – 0.5 dex. In Section 4.1 we showed that the nominal model is consistent with the binned column densities in our data set, and steeper profiles are in tension with the average observed distribution of the metal ions. We note that these results are for a metallicity that is constant with r. The tension between models with $a_f > 0$ and the data can be alleviated with a metallicity profile that increases with the distance from the galaxy (see also P17).

It is also possible to consider $f_{V,cool}$ that increases with radius, following recent accretion of cool gas onto the halo, either through smooth accretion from the IGM, or gas stripping as part of minor mergers. An increasing $f_{V,cool}$ will give flatter column density profiles, which may also be in tension with the binned measured columns. This tension can then be alleviated with a metallicity profile that decreases with radial distance, similar to the FSM20 fiducial warm/hot gas model. We plan to explore these scenarios in more detail in future work.

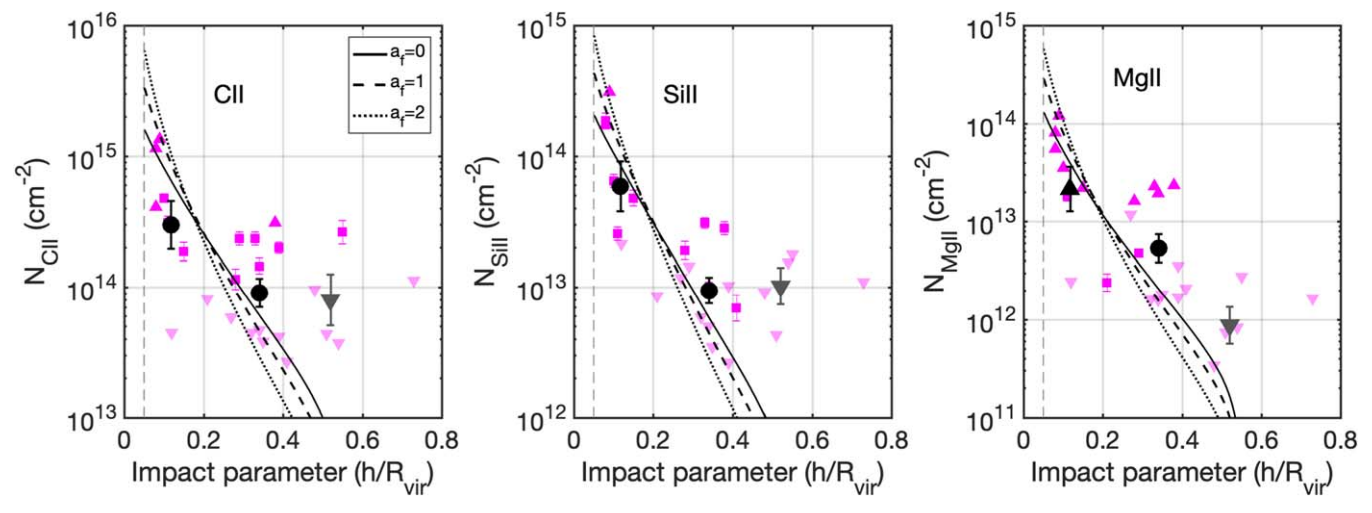


Figure C1. C II, Si II, and Mg II (left to right) column densities for models with a cool gas volume filling fraction that varies as $f_{\text{V,cool}} \propto r^{-af}$. Models with $a_f = 1$ and $a_f = 2$ (dashed and dotted curves, respectively) produce steeper column density functions than the nominal model presented in Section 4 ($a_f = 0$, solid curve) and are in tension with the binned data.

ORCID iDs

Yakov Faerman https://orcid.org/0000-0003-3520-6503 Jessica K. Werk https://orcid.org/0000-0002-0355-0134

References

```
Afruni, A., Fraternali, F., & Pezzulli, G. 2019, A&A, 625, A11
Afruni, A., Fraternali, F., & Pezzulli, G. 2021, MNRAS, 501, 5575
Afruni, A., Pezzulli, G., & Fraternali, F. 2022, MNRAS, 509, 4849
Appleby, S., Davé, R., Sorini, D., Storey-Fisher, K., & Smith, B. 2021,
    INRAS, 507, 2383
Armillotta, L., Fraternali, F., Werk, J. K., Prochaska, J. X., & Marinacci, F.
   2017, MNRAS, 470, 114
Asplund, M., Grevesse, N., Sauval, A. J., & Scott, P. 2009, ARA&A, 47, 481
Augustin, R., Péroux, C., Hamanowicz, A., et al. 2021, MNRAS, 505, 6195
Barbani, F., Pascale, R., Marinacci, F., et al. 2023, MNRAS, 524, 4091
Berg, M. A., Lehner, N., Howk, J. C., et al. 2023, ApJ, 944, 101
Bolatto, A. D., Warren, S. R., Leroy, A. K., et al. 2013, Natur, 499, 450
Bordoloi, R., Lilly, S. J., Kacprzak, G. G., et al. 2014, ApJ, 784, 108
Bordoloi, R., Lilly, S. J., Knobel, C., et al. 2011, ApJ, 743, 10
Bordoloi, R., Tumlinson, J., Werk, J. K., et al. 2014, ApJ, 796, 136
Borisova, E., Cantalupo, S., Lilly, S. J., et al. 2016, ApJ, 831, 39
Borthakur, S., Heckman, T., Tumlinson, J., et al. 2015, ApJ, 813, 46
Bregman, J. N., & Lloyd-Davies, E. J. 2007, ApJ, 669, 990
Burchett, J. N., Tripp, T. M., Prochaska, J. X., et al. 2019, ApJL, 877, L20
Butsky, I. S., Fielding, D. B., Hayward, C. C., et al. 2020, ApJ, 903, 77
Cai, Z., Hamden, E., Matuszewski, M., et al. 2018, ApJL, 861, L3
Cantalupo, S., Arrigoni-Battaia, F., Prochaska, J. X., Hennawi, J. F., &
   Madau, P. 2014, Natur, 506, 63
Charlton, J. C., & Churchill, C. W. 1998, ApJ, 499, 181
Chen, H.-W., Helsby, J. E., Gauthier, J.-R., et al. 2010, ApJ, 714, 1521
Chen, H.-W., Zahedy, F. S., Boettcher, E., et al. 2020, MNRAS, 497, 498
Chen, H.-W., Zahedy, F. S., Johnson, S. D., et al. 2018, MNRAS, 479, 2547
Chisholm, J., Tremonti, C. A., Leitherer, C., & Chen, Y. 2017, MNRAS,
   469, 4831
Chomiuk, L., & Povich, M. S. 2011, AJ, 142, 197
Christensen, C. R., Davé, R., Governato, F., et al. 2016, ApJ, 824, 57
Churchill, C. W., Mellon, R. R., Charlton, J. C., et al. 2000, ApJS, 130, 91
Correa, C. A., Wyithe, J. S. B., Schaye, J., & Duffy, A. R. 2015, MNRAS,
  450, 1521
Damle, M., Sparre, M., Richter, P., et al. 2022, MNRAS, 512, 3717
Dekel, A., Birnboim, Y., Engel, G., et al. 2009, Natur, 457, 451
Esmerian, C. J., Kravtsov, A. V., Hafen, Z., et al. 2021, MNRAS, 505, 1841
Evans, J. L., Churchill, C. W., Murphy, M. T., Nielsen, N. M., & Klimek, E. S.
   2013, ApJ, 768, 3
Faerman, Y., Pandya, V., Somerville, R. S., & Sternberg, A. 2022, ApJ,
  928, 37
Faerman, Y., Sternberg, A., & McKee, C. F. 2017, ApJ, 835, 52
Faerman, Y., Sternberg, A., & McKee, C. F. 2020, ApJ, 893, 82
Fakhouri, O., Ma, C.-P., & Boylan-Kolchin, M. 2010, MNRAS, 406, 2267
Fang, T., Buote, D., Bullock, J., & Ma, R. 2015, ApJS, 217, 21
Faucher-Giguère, C.-A., Lidz, A., Zaldarriaga, M., & Hernquist, L. 2009, ApJ,
   703, 1416
Ferland, G. J., Chatzikos, M., Guzmán, F., et al. 2017, RMxAA, 53, 385
Fielding, D. B., & Bryan, G. L. 2022, ApJ, 924, 82
Fielding, D. B., Ostriker, E. C., Bryan, G. L., & Jermyn, A. S. 2020, ApJL,
   894, L24
Fox, A. J., Richter, P., Ashley, T., et al. 2019, ApJ, 884, 53
Fraternali, F. 2017, in Astrophysics and Space Science Library, Vol. 430, Gas
   Accretion onto Galaxies, ed. A. Fox & R. Davé (Cham: Springer), 323
Giovanelli, R., Haynes, M. P., Adams, E. A. K., et al. 2013, AJ, 146, 15
Gnat, O., & Sternberg, A. 2004, ApJ, 608, 229
Gronke, M., & Oh, S. P. 2020, MNRAS, 494, L27
Gronke, M., Oh, S. P., Ji, S., & Norman, C. 2022, MNRAS, 511, 859
Gupta, A., Mathur, S., Krongold, Y., Nicastro, F., & Galeazzi, M. 2012, ApJL,
   756, L8
Haardt, F., & Madau, P. 2012, ApJ, 746, 125
Hafen, Z., Faucher-Giguère, C.-A., Anglés-Alcázar, D., et al. 2019, MNRAS,
Hafen, Z., Sameer, Hummels, C., et al. 2023, arXiv:2305.01842
Haislmaier, K. J., Tripp, T. M., Katz, N., et al. 2021, MNRAS, 502, 4993
Heckman, T. M., Norman, C. A., Strickland, D. K., & Sembach, K. R. 2002,
   ApJ, 577, 691
Hennawi, J. F., & Prochaska, J. X. 2013, ApJ, 766, 58
Ho, S. H., & Martin, C. L. 2020, ApJ, 888, 14
```

```
Ho, S. H., Martin, C. L., Kacprzak, G. G., et al. 2017, ApJ, 835, 267
Holguin, F. 2022, PhD thesis, Horace H. Rackham School of Graduate Studies,
  https://deepblue.lib.umich.edu/handle/2027.42/174621
Hopkins, P. F., Chan, T. K., Garrison-Kimmel, S., et al. 2020, MNRAS,
  492, 3465
Hummels, C. B., Smith, B. D., Hopkins, P. F., et al. 2019, ApJ, 882, 156
Ji, S., Chan, T. K., Hummels, C. B., et al. 2020, MNRAS, 496, 4221
Ji, S., Oh, S. P., & Masterson, P. 2019, MNRAS, 487, 737
Johnson, S. D., Chen, H.-W., & Mulchaey, J. S. 2015, MNRAS, 449, 3263
Joung, M. R., Bryan, G. L., & Putman, M. E. 2012a, ApJ, 745, 148
Joung, M. R., Putman, M. E., Bryan, G. L., Fernández, X., & Peek, J. E. G.
  2012b, ApJ, 759, 137
Kacprzak, G. G., Churchill, C. W., Barton, E. J., et al. 2011, ApJ, 733, 105
Kacprzak, G. G., Churchill, C. W., Ceverino, D., et al. 2010, ApJ, 711, 533
Keeney, B. A., Stocke, J. T., Danforth, C. W., et al. 2017, ApJS, 230, 6
Kelly, A. J., Jenkins, A., Deason, A., et al. 2022, MNRAS, 514, 3113
Kereš, D., Katz, N., Weinberg, D. H., & Davé, R. 2005, MNRAS, 363, 2
Khaire, V., & Srianand, R. 2019, MNRAS, 484, 4174
Kim, C.-G., Ostriker, E. C., Somerville, R. S., et al. 2020, ApJ, 900, 61
Klypin, A., Zhao, H., & Somerville, R. S. 2002, ApJ, 573, 597
Lan, T.-W., & Mo, H. 2019, MNRAS, 486, 608
Lehner, N., Berek, S. C., Howk, J. C., et al. 2020, ApJ, 900, 9
Lehner, N., Kopenhafer, C., O'Meara, J. M., et al. 2022, ApJ, 936, 156
Lehner, N., O'Meara, J. M., Fox, A. J., et al. 2014, ApJ, 788, 119
Li, M., & Bryan, G. L. 2020, ApJL, 890, L30
Licquia, T. C., & Newman, J. A. 2015, ApJ, 806, 96
Lochhaas, C., Thompson, T. A., Quataert, E., et al. 2018, MNRAS, 481, 1873
Maller, A. H., & Bullock, J. S. 2004, MNRAS, 355, 694
Mandelker, N., Dekel, A., Ceverino, D., et al. 2017, MNRAS, 464, 635
Marinacci, F., Binney, J., Fraternali, F., et al. 2010, in AIP Conf. Ser. 1240,
  Hunting for the Dark: the Hidden Side of Galaxy Formation, ed.
   V. P. Debattista & C. C. Popescu (Melville, NY: AIP), 166
Martin, C. L., Shapley, A. E., Coil, A. L., et al. 2012, ApJ, 760, 127
Matejek, M. S., & Simcoe, R. A. 2012, ApJ, 761, 112
Mathews, W. G., & Prochaska, J. X. 2017, ApJL, 846, L24
McCourt, M., Oh, S. P., O'Leary, R., & Madigan, A.-M. 2018, MNRAS,
  473, 5407
McCourt, M., Sharma, P., Quataert, E., & Parrish, I. J. 2012, MNRAS,
  419, 3319
McQuinn, M., & Werk, J. K. 2018, ApJ, 852, 33
Mitchell, P. D., Schaye, J., Bower, R. G., & Crain, R. A. 2020, MNRAS,
  494, 3971
Nateghi, H., Kacprzak, G. G., Nielsen, N. M., et al. 2021, MNRAS,
  500, 3987
Neeleman, M., Prochaska, J. X., & Wolfe, A. M. 2015, ApJ, 800, 7
Neeleman, M., Prochaska, J. X., Zwaan, M. A., et al. 2016, ApJL, 820, L39
Nelson, D., Kauffmann, G., Pillepich, A., et al. 2018, MNRAS, 477, 450
Nelson, D., Sharma, P., Pillepich, A., et al. 2020, MNRAS, 498, 2391
Nielsen, N. M., Churchill, C. W., & Kacprzak, G. G. 2013, ApJ, 776, 115
Ocker, S. K., Cordes, J. M., & Chatterjee, S. 2021, ApJ, 911, 102
Oppenheimer, B. D. 2018, MNRAS, 480, 2963
Oppenheimer, B. D., Schaye, J., Crain, R. A., Werk, J. K., & Richings, A. J.
  2018a, MNRAS, 481, 835
Oppenheimer, B. D., Segers, M., Schaye, J., Richings, A. J., & Crain, R. A.
  2018b, MNRAS, 474, 4740
Pandya, V., Fielding, D. B., Anglés-Alcázar, D., et al. 2021, MNRAS,
  508, 2979
Peeples, M. S., Corlies, L., Tumlinson, J., et al. 2019, ApJ, 873, 129
Piacitelli, D. R., Solhaug, E., Faerman, Y., & McQuinn, M. 2022, MNRAS,
  516, 3049
Prochaska, J. X., Weiner, B., Chen, H.-W., Mulchaey, J., & Cooksey, K. 2011,
   ApJ, 740, 91
Prochaska, J. X., Werk, J. K., Worseck, G., et al. 2017, ApJ, 837, 169
Prochter, G. E., Prochaska, J. X., & Burles, S. M. 2006, ApJ, 639, 766
Putman, M. E., Peek, J. E. G., & Joung, M. R. 2012, ARA&A, 50, 491
Putman, M. E., Zheng, Y., Price-Whelan, A. M., et al. 2021, ApJ, 913, 53
Qu, Z., & Bregman, J. N. 2018a, ApJ, 862, 23
Qu, Z., & Bregman, J. N. 2018b, ApJ, 856, 5
Qu, Z., Chen, H.-W., Rudie, G. C., et al. 2022, MNRAS, 516, 4882
Ramesh, R., Nelson, D., Heesen, V., et al. 2023a, arXiv:2305.11214
Ramesh, R., Nelson, D., & Pillepich, A. 2023b, MNRAS, 518, 5754
Ramesh, R., Nelson, D., & Pillepich, A. 2023c, MNRAS, 522, 1535
Ribaudo, J., Lehner, N., Howk, J. C., et al. 2011, ApJ, 743, 207
Rigby, J. R., Charlton, J. C., & Churchill, C. W. 2002, ApJ, 565, 743
Roca-Fàbrega, S., Dekel, A., Faerman, Y., et al. 2019, MNRAS, 484, 3625
Rubin, K. H. R., Diamond-Stanic, A. M., Coil, A. L., Crighton, N. H. M., &
  Stewart, K. R. 2018, ApJ, 868, 142
```

```
Rubin, K. H. R., Hennawi, J. F., Prochaska, J. X., et al. 2015, ApJ, 808, 38
Rubin, K. H. R., Juarez, C., Cooksey, K. L., et al. 2022, ApJ, 936, 171
Rudie, G. C., Steidel, C. C., Pettini, M., et al. 2019, ApJ, 885, 61
Rudie, G. C., Steidel, C. C., Shapley, A. E., & Pettini, M. 2013, ApJ, 769, 146
Rupke, D. S., Veilleux, S., & Sanders, D. B. 2005, ApJS, 160, 115
Ryan-Weber, E. V., Begum, A., Oosterloo, T., et al. 2008, MNRAS, 384, 535
Sameer, Charlton, J. C., Norris, J. M., et al. 2021, MNRAS, 501, 2112
Sarkar, K. C., Sternberg, A., & Gnat, O. 2022, ApJ, 940, 44
Sharma, P., McCourt, M., Quataert, E., & Parrish, I. J. 2012, MNRAS,
  420, 3174
Shull, J. M., & Moss, J. A. 2020, ApJ, 903, 101
Somerville, R. S., Hopkins, P. F., Cox, T. J., Robertson, B. E., & Hernquist, L.
   2008, MNRAS, 391, 481
Somerville, R. S., Popping, G., & Trager, S. C. 2015, MNRAS, 453, 4337
Somerville, R. S., & Primack, J. R. 1999, MNRAS, 310, 1087
Sparre, M., Pfrommer, C., & Ehlert, K. 2020, MNRAS, 499, 4261
Sparre, M., Pfrommer, C., & Vogelsberger, M. 2019, MNRAS, 482, 5401
Steidel, C. C., & Sargent, W. L. W. 1992, ApJS, 80, 1
Stern, J., Faucher-Giguère, C.-A., Hennawi, J. F., et al. 2018, ApJ, 865, 91
Stern, J., Fielding, D., Faucher-Giguère, C.-A., & Quataert, E. 2019, MNRAS,
   488, 2549
Stern, J., Hennawi, J. F., Prochaska, J. X., & Werk, J. K. 2016, ApJ, 830, 87
Sternberg, A., McKee, C. F., & Wolfire, M. G. 2002, ApJS, 143, 419
Stocke, J. T., Keeney, B. A., Danforth, C. W., et al. 2013, ApJ, 763, 148
Tan, B., & Fielding, D. B. 2023, arXiv:2305.14424
Tan, B., & Oh, S. P. 2021, MNRAS, 508, L37
Tan, B., Oh, S. P., & Gronke, M. 2021, MNRAS, 502, 3179
Tan, B., Oh, S. P., & Gronke, M. 2023, MNRAS, 520, 2571
```

Tchernyshyov, K., Werk, J. K., Wilde, M. C., et al. 2022, ApJ, 927, 147

```
Tchernyshyov, K., Werk, J. K., Wilde, M. C., et al. 2023, ApJ, 949, 41
Tejos, N., López, S., Ledoux, C., et al. 2021, MNRAS, 507, 663
Tollet, É., Cattaneo, A., Macciò, A. V., Dutton, A. A., & Kang, X. 2019,
  MNRAS, 485, 2511
Tonnesen, S., & Bryan, G. L. 2009, ApJ, 694, 789
Tripp, T. M. 2022, MNRAS, 511, 1714
Tumlinson, J., Peeples, M. S., & Werk, J. K. 2017, ARA&A, 55, 389
Tumlinson, J., Thom, C., Werk, J. K., et al. 2011, Sci, 334, 948
Tumlinson, J., Thom, C., Werk, J. K., et al. 2013, ApJ, 777, 59
Upton Sanderbeck, P. R., McQuinn, M., D'Aloisio, A., & Werk, J. K. 2018,
   ApJ, 869, 159
van de Voort, F., Springel, V., Mandelker, N., van den Bosch, F. C., &
  Pakmor, R. 2019, MNRAS, 482, L85
Vedantham, H. K., & Phinney, E. S. 2019, MNRAS, 483, 971
Veilleux, S., Maiolino, R., Bolatto, A. D., & Aalto, S. 2020, A&ARv, 28, 2
Voit, G. M. 2019, ApJ, 880, 139
Werk, J. K., Prochaska, J. X., Thom, C., et al. 2012, ApJS, 198, 3
Werk, J. K., Prochaska, J. X., Thom, C., et al. 2013, ApJS, 204, 17
Werk, J. K., Prochaska, J. X., Tumlinson, J., et al. 2014, ApJ, 792, 8
Werk, J. K., Rubin, K. H. R., Bish, H. V., et al. 2019, ApJ, 887, 89
Wilde, M. C., Werk, J. K., Burchett, J. N., et al. 2021, ApJ, 912, 9
Wotta, C. B., Lehner, N., Howk, J. C., et al. 2019, ApJ, 872, 81
Wotta, C. B., Lehner, N., Howk, J. C., O'Meara, J. M., & Prochaska, J. X.
Wright, R. J., Lagos, C. d. P., Power, C., & Correa, C. A. 2021, MNRAS,
  504, 5702
Zahedy, F. S., Chen, H.-W., Cooper, T. M., et al. 2021, MNRAS, 506, 877
Zahedy, F. S., Chen, H.-W., Johnson, S. D., et al. 2019, MNRAS, 484, 2257
Zheng, Y., Faerman, Y., Oppenheimer, B. D., et al. 2023, arXiv:2301.12233
```